

Effects of Various Fillet Shapes on a 76/40 Double Delta Wing from Mach 0.18 to 0.7

Mr. Hugo A. Gonzalez
Air 4.3.2.2, Building 2187
Suite 1320B, Unit 5, NAVAIRSYSCOHQ
48110 Shaw Road
Patuxent River, MD 20670-1906, USA

Dr. Blair G. McLachlan
NASA Ames Research Center
M/S 247-2, Building 247, Room 110A
Moffet Field, CA 94035, USA

Mr. Gary E. Erickson
NASA Langley Research Center
M/S 413, Building 1251, Room 125
Hampton, VA 23681, USA

Dr. James H. Bell
NASA Ames Research Center
M/S 620-1, Building 260, Room 114
Moffet Field, CA 94035, USA

ABSTRACT

The effects of linear, diamond, and parabolic fillets on a double delta wing were investigated in the NASA Langley 7x10ft High Speed Tunnel from Mach 0.18 to 0.7 and angles of attack from -4° to 42° . Force and moment, pneumatic pressures, pressure sensitive paint, and vapor screen flow visualization measurements were used to characterize the flow field and to determine longitudinal forces and moments. The fillets increased lift coefficient and reduced induced drag without significantly affecting pitching moment. Pressure sensitive paint showed the increase in lift is caused by an increase in suction and broadening of the vortex suction footprint. Vapor screen results showed the mixing and coalescing of the strake fillet and wing vortices causes the footprint to broaden.

Nomenclature

b	Span (inches)	$C_{p,u}$	Upper surface pressure coefficient
BL	Buttline (inches)	MS	Model station (inches)
c	Root chord (inches)	L/D	Lift-to-drag ratio
C_D	Drag coefficient	Re	Reynolds number based on root chord
C_L	Lift coefficient	x	Streamwise coordinate (inches)
C_m	Pitching moment coefficient at 73.27% root chord location	y	Spanwise coordinate (inches)
		α	Angle of attack (degrees)

INTRODUCTION

The subsonic and transonic high angle-of-attack flow fields about advanced aircraft configurations (F/A-18, F-16, YF-22, YF-23, X-31, and JSF) are characterized by separation induced vortical flows, mutual interactions of multiple vortices, vortex breakdown, and interactions of the vortex flows with shock waves and control surfaces. The shedding of vortices on aircraft occur at the forebody, moderate to highly swept wing leading edges, strakes and leading edge extensions (LEX), and the junction of aerodynamic surfaces with each other and the fuselage. The shedding, interaction, and breakdown of these vortices are highly sensitive to both the aircraft's geometry and the flow conditions. In addition to producing the benefits of enhanced lift and maneuverability, the vortical flow also causes serious flight path departure and structural fatigue problems.^{1, 2} The ability to control the trajectory, strength, and breakdown processes of the vortices may not only alleviate the problems generated by this flow phenomena, but may also enhance the controllability, maneuverability, and agility of the aircraft.

Report Documentation Page

Form Approved
OMB No. 0704-0188

Public reporting burden for the collection of information is estimated to average 1 hour per response, including the time for reviewing instructions, searching existing data sources, gathering and maintaining the data needed, and completing and reviewing the collection of information. Send comments regarding this burden estimate or any other aspect of this collection of information, including suggestions for reducing this burden, to Washington Headquarters Services, Directorate for Information Operations and Reports, 1215 Jefferson Davis Highway, Suite 1204, Arlington VA 22202-4302. Respondents should be aware that notwithstanding any other provision of law, no person shall be subject to a penalty for failing to comply with a collection of information if it does not display a currently valid OMB control number.

1. REPORT DATE 00 MAR 2003	2. REPORT TYPE N/A	3. DATES COVERED -	
4. TITLE AND SUBTITLE Effects of Various Fillet Shapes on a 76/40 Double Delta Wing from Mach 0.18 to 0.7		5a. CONTRACT NUMBER	
		5b. GRANT NUMBER	
		5c. PROGRAM ELEMENT NUMBER	
6. AUTHOR(S)		5d. PROJECT NUMBER	
		5e. TASK NUMBER	
		5f. WORK UNIT NUMBER	
7. PERFORMING ORGANIZATION NAME(S) AND ADDRESS(ES) NATO Research and Technology Organisation BP 25, 7 Rue Anelle, F-92201 Neuilly-Sue-Seine Cedex, France		8. PERFORMING ORGANIZATION REPORT NUMBER	
9. SPONSORING/MONITORING AGENCY NAME(S) AND ADDRESS(ES)		10. SPONSOR/MONITOR'S ACRONYM(S)	
		11. SPONSOR/MONITOR'S REPORT NUMBER(S)	
12. DISTRIBUTION/AVAILABILITY STATEMENT Approved for public release, distribution unlimited			
13. SUPPLEMENTARY NOTES Also see: ADM001490, Presented at RTO Applied Vehicle Technology Panel (AVT) Symposium held inLeon, Norway on 7-11 May 2001, The original document contains color images.			
14. ABSTRACT			
15. SUBJECT TERMS			
16. SECURITY CLASSIFICATION OF:			17. LIMITATION OF ABSTRACT
a. REPORT unclassified	b. ABSTRACT unclassified	c. THIS PAGE unclassified	UU
			18. NUMBER OF PAGES 40
			19a. NAME OF RESPONSIBLE PERSON

Because of the complexity and potential benefit from vortical flow, research has and is being conducted in this field to improve the understanding of the shedding, interaction, and breakdown processes of vortex flow.³⁻¹³ This research has identified techniques for controlling vortical flows which provide additional aerodynamic augmentation, complementing conventional control surfaces. These techniques potentially enhance an aircraft's operating envelope and maneuverability.

The objective of this experimental investigation was to understand the impact of small geometry modifications (fillets) at the juncture of a 76° sweep leading edge extension (LEX) or strake and a 40° sweep cropped delta wing ("76/40 double delta wing"). A sharp leading edge model was used to depict a generic fighter strake and wing configuration. These fillets were developed to control the shedding, trajectory, and subsequent breakdown of vortices to enhance aircraft aerodynamic performance at subsonic and transonic speeds, and at elevated angles of attack. Longitudinal, lateral, and flow field characteristics of the double delta wing were investigated with different size linear, diamond, and parabolic shape fillets, Figures 1 and 2. The investigation was conducted in the 7x10 Ft. High Speed Tunnel at the National Aeronautics and Space Administration's (NASA) Langley Research Center (LaRC). The wind tunnel test was conducted from Mach 0.18 to 0.7; Reynolds numbers per foot from 1.2 to 3.6 x 10⁶; angles of attack from -4° to 42°; and zero sideslip. The presentation of the experimental results begins with a description of the aerodynamic characteristics of the baseline 76/40 double delta wing. With the baseline configuration as a basis for a comparison, a discussion of the effects of the various fillets follows.

BACKGROUND

It is believed that by affecting the shedding process at the junction of the strake and wing, the trajectory, vortex-to-vortex interaction, and breakdown of the resulting vortex structure may be controlled resulting in enhanced lift and longitudinal control. Through asymmetric deployment of the fillets, additional lateral-directional control may be realized. The fillets are envisioned as being deployable or fixed at the junction of the strake (LEX) and wing. If deployable during maneuvering or landing approach, these fillets could enhance aerodynamic performance on demand.

DOUBLE DELTA WING VORTEX FLOW FIELD

Several researchers have investigated the fundamental flow field of double delta wings with sharp leading edges. Cunningham and van Boer,⁷ Brennenstuhl and Hummel,⁸ Thompson,¹¹ Kern,^{14,15} and Ekaterinaris et al.¹⁶ have conducted studies on double delta wings with various strake and wing leading edge sweeps. All the above studies had comparable results for similar leading edge sweeps.

The flow field generated by a double delta wing configuration can be fundamentally categorized as follows. At low angles of attack, the strake and wing generate their own distinct set of vortices that tend to follow the strake and wing leading edges. Starting at the strake wing juncture, the strake vortex continues downstream no longer being fed by the vortex sheet from the strake, and the wing generates a new stronger vortex (with increased circulation) than the strake vortex.¹⁷ As angle of attack increases, the wing vortex starts to move inboard away from the wing leading edge. With increasing angle of attack, a point is reached where the wing vortex entrains the strake vortex and the two vortices begin to coalesce. Depending on wing sweep, the wing vortex may breakdown (burst) before the strake and wing vortices begin to coalesce. At higher angles of attack, both the wing and strake vortices burst: the wing vortex burst point travels upstream with increasing angle of attack, eventually reaching the strake/wing junction, and the strake vortex burst point moves up stream until it reaches the apex of the strake.

VORTEX FLOW CONTROL HISTORY

The concept of flow control through vortex manipulation is not a new topic. H.R. Lawrence, in 1950, suggested the use of asymmetric edge shape effects to achieve roll control of low aspect ratio wings at high angles of attack.⁴ In the 60's and 70's leading edge extensions (LEX) or strakes were developed and used in the development of F-5A/B, YF-17, F-16, and F/A-18. Several geometric modification concepts have been

suggested by Lamar,¹⁸ Rao,^{19,20} Bobbitt and Foughner,²¹ and Malcolm.²² Their concepts range from devices to enhance lift for landing and maneuvering to improving stability and control (i.e. hinged strakes, vortex flap, apex flap, leading edge vortex generator, etc.). Kern^{14,15} provides a comprehensive history of vortex flow control.

A computational investigation on the effect of the fillets presented in this paper was conducted by Kern.^{14,15} Straka,²³ while investigating the effects of wing planform on vortex break down, developed concave fillets similar to the parabolic fillets developed by the Naval Air Systems Command and Office of Naval Research "Vortex Flow Control" program. The Naval Postgraduate School conducted a water tunnel test to investigate the highly interactive vortical flow field generated by the fillets presented in this paper.²⁴

EXPERIMENTAL INVESTIGATION

The wind tunnel test was conducted with a model that represents a generic fighter or high speed civil transport strake and wing planform. The model, presented in Figure 1, is comprised of a flat plate cropped double delta wing planform with a 76° strake (LEX) and a 40° wing. The strake and wing leading edges are beveled 20° and sharp. The chord and wing span are 16.000 and 16.326 inches, respectively. The strake/wing juncture is located at MS 8.933 and BL 2.227; the cropped portion of the wing begins at MS 13.46 and BL 8.163. (Model station measurements begin at the nose tip.) The model is 0.375 inches thick.

To control the vortex flow, three fillet shapes (linear, diamond, and parabolic) were employed at the strake and wing juncture of the baseline configuration. The linear and diamond fillets added additional discontinuities, from which additional vortices were expected to originate, while parabolic fillets removed the discontinuity of the junction. Three fillet sizes based on total fillet area (left and right) to model reference area were tested; 0.5%, 1%, and 2.5% for linear and diamond, and 0.5%, and 1% for parabolic. (A 2.5% parabolic fillet was too large to fit on the model.) The various 1% fillets are illustrated in Figure 2. Both symmetrical and asymmetric fillets were tested. However, only symmetrical data is presented in this paper.

The data consisted of model force, moment, surface static pressures derived from taps and pressure sensitive paint, and laser vapor screen. Six component forces and moments were measured with a fairing covered bottom-mounted sting balance. The moment reference center (MRC) of the double delta wing was located at 73.27% of the root chord. This MRC coincides that used in References 7 and 15 on a similar double delta wing planform. Balance pitch attitude was measured with an accelerometer mounted near the sting pivot point of the model support system. Roll was determined with a potentiometer installed in the model support system. All angle measurements were corrected for balance and sting deflections. Forty-seven surface static pressure orifices (taps) were used during the test. They were distributed in three spanwise rows on the left-hand side of the wing upper surface. The spanwise rows were located at $x/c = 0.25, 0.75, \text{ and } 0.9$. A forty-eight ESP module house in the fairing forward of the balance was used to measure orifice pressures.

PRESSURE SENSITIVE PAINT

To supplement the surface pressure orifice data, the pressure sensitive paint (PSP) method in References 25 and 26 was employed. A platinum octaethylporphyrin-based luminescent pressure sensitive paint developed by NASA Ames Research Center and The University of Washington was applied to the upper surface of the model. The painted model was illuminated by six ultraviolet (UV) lamps and imaged by an 8-bit CCD camera mounted above the test section ceiling. The wind-off and wind-on images were registered and resectioned into a planform view pressure map by software developed at NASA Ames.²⁷ The paint was applied to the entire upper surface of the wing, except along the pressure tap rows, which appear as black bands in the pressure map images. PSP and pressure tap data were taken simultaneously. Measurements from pressure taps were taken with and without PSP to determine the paint thickness and texture effects on the data. PSP surface finish effects on pneumatic data were small (less than a C_p of 0.07). The PSP was calibrated with an *In Situ* technique.²⁵ To calibrate the PSP, the paint intensity ratio in front and aft of each black band were correlated to corresponding pressure tap data. Since a delta wing vortex pressure footprint has a chord

span gradient, some small errors are introduced by this technique. Hence, the pressure tap data should be treated as quantitative while the PSP pressure map images should be treated as qualitative. All upper surface static pressure orifice values presented in this paper were taken without pressure sensitive paint on the model. The PSP system used in this test had insufficient signal-to-noise ratio to make effective measurements below Mach 0.3. In addition, no lower surface PSP data were obtained due to time and equipment constraints.

FLOW VISUALIZATION

In addition to force, moment, and pressure measurements, off-body flow visualization was conducted with a vapor screen technique.²⁸ The ambient relative humidity in the test section created condensation within the vortical flow of the model. Cross-sections of the vortices were illuminated with a laser light sheet revealing bright vortices with a dark background. Light sheet position was varied remotely to provide coverage of the model. The light sheet optics were located above the test section ceiling. The off body flow field features were recorded by video cameras mounted on the sting and outside the test section.

WIND TUNNEL FACILITY AND TEST CONDITIONS

The data were obtained in the 7x10 Ft. High Speed Tunnel (HST) at NASA Langley Research Center in Hampton, Virginia. The 7x10 Ft. HST was a continuous-flow, closed circuit, and atmospheric facility capable of operating to Mach 0.8. A complete description of the HST is provided in Reference 29.

The test was conducted at free stream Mach numbers 0.18, 0.3, 0.5, and 0.7 and angles of attack from -4.0° to 42.0° . Balance limits restricted the angle of attack to approximately 28° and 16° at Mach 0.5 and 0.7, respectively. No sideslip conditions were investigated. The tunnel stagnation pressure was set by atmospheric conditions. The Reynolds numbers per foot were approximately 1.2, 2.0, 3.0, and 3.6×10^6 . No base or balance cavity pressures were measured. Solid blockage and wall constraint corrections were applied.^{30, 31} The strake, wing, balance fairing, and fillets were tested with free boundary layer transition.

DISCUSSION OF RESULTS

BASELINE MODEL LONGITUDINAL AND FLOW FIELD CHARACTERISTICS

Baseline Longitudinal Characteristics

The baseline double delta wing longitudinal characteristics at $M=0.18$, 0.3, 0.5, and 0.7 are presented in Figure 3. The lift, drag, and pitching moment coefficients for $M=0.18$ and 0.3 are characterized by two points where there is a slope change (break). The first slope break is associated with the wing vortex bursting at or near the wing trailing edge. The second slope change (stall) is associated with the strake vortex bursting close to the strake's apex. At $M=0.18$ and 0.3, the first slope change occurs at an angle of attack of 14° rather than at 16° for $M=0.5$. The $M=0.5$ lift curve collapses onto the $M=0.18$ and 0.3 curves at 24° . The $M=0.7$ data does not change slope abruptly between -4° to 16° angle of attack. A lift slope increase associated with compressibility is observed at Mach 0.5 and 0.7. Pitching moment stability also increases with increasing Mach. A pitch-up associated with the wing vortex bursting occurs at the first lift break. Pitching moment decreases along the same curve after the strake vortex bursts. Table 1 summarizes these longitudinal characteristics. Baseline repeatability is shown in Figure 4. Data repeated well below 16° angle of attack. Above 16° angle of attack the data repeated with varying level of success. It is not known if Reynolds number variations or slight inconsistencies in model changes cause the data scatter at higher angles of attack.

Mach	Values at First Break Point				Values at Second Break Point (Stall)			
	Alpha	C_L	C_D	C_m	Alpha	C_{Lmax}	C_D	C_m
0.18	14°	0.625	0.2	0.075	36°	0.87	0.74	0.137
0.30	14°	0.6	0.2	0.075	36°	0.82	0.7	0.125
0.50	16°	0.7	0.25	0.076	N/A	N/A	N/A	N/A
0.70	N/A	N/A	N/A	N/A	N/A	N/A	N/A	N/A

Table 1- Longitudinal Data Slope Change (Break) Points

Baseline Flow Field Characteristics

Figures 5 and 6 present corresponding surface pressure distribution plots and PSP pressure maps at Mach 0.5 and 0.7. In the PSP pressure maps, low-pressure regions (and thus vortex footprints on the surface) are shown in yellow, green, and blue, while high-pressure regions are purple and red. Vapor screen images supplement the pressure data. (In the vapor screen images, the model surface is reflective; this second, reflected image of the vortices can be seen below the bright horizontal line indicating the contact of the light sheet with the model surface.) At Mach 0.5 and 10° angle of attack, the strake and wing vortices coexist as individual vortices with no mixing. At 14° angle of attack, the wing and strake vortices are mixing/intertwining near the trailing edge: two distinct footprints are seen at x/c of 0.75, however, the footprint present at a x/c of 0.9 indicates the wing and strake vortices fully coalesced. As angle of attack is increased, the strake and wing vortex pressure footprints coalesce into a single footprint and bursting is indicated further upstream. At 20° angle of attack, a single vortex pressure footprint is present at a x/c of 0.75 and 0.9. The PSP data shows the wing vortex generates a large amount of suction near the wing/strake juncture. Mach 0.7 data depicted in Figure 6, shows two distinct strake and wing vortices up to 16° angle of attack. The pressure footprints from the wing vortices appear diffused, indicating the wing vortices may be bursting. The Mach 0.7 PSP pressure maps show striations in the strake vortex pressure footprint. The striation pattern has the wrong orientation to be the high and low suction peaks associated with the shear layer instability roll up shown in Reference 12, Figure 16 and in Reference 32, Figures 3.22 and 3.23. As depicted in References 5 through 16, the near surface flow under a vortex proceeds in a downstream and spanwise outboard direction. The striations observed here are perpendicular to the near surface flow under a vortex, supporting the hypothesis that the striations are caused by localized shock waves and subsequent pressure recovery. Along with the striations the vapor screen images show a ring of condensation around the primary condensations pattern of the strake vortex. It is not known if this is a connecting vortex sheet between the strake and wing vortex sheets.

FILLET EFFECTS ON LONGITUDINAL AND FLOW FIELD CHARACTERISTICS

Fillet Geometry Effects

In general it was observed that the linear, diamond and parabolic fillets increase lift and reduce drag for a given C_L . The diamond and linear fillets have a small effect on pitching moment. The parabolic fillets delay pitch-up. However, the parabolic fillets pitch-up is larger than the other fillets or the baseline configuration. The linear fillet increases C_L from 2.9% to 28.6%. The diamond fillet increases C_L from 2.9% to 17.9%. The parabolic fillet increases C_L from 20% to 39.3% depending on angle of attack, Mach and fillet size. Post stall fillet data collapses on the baseline post stall data. This is caused by the strake vortex bursting at the model apex.

- $M = 0.18$

A comparison of the 0.5% linear, diamond, and parabolic fillets to the baseline configuration at Mach 0.18 is provided in Figure 7. The parabolic fillet generates a higher lift coefficient and lower drag, for a given C_L , after 12° angle of attack as compared to the baseline. The parabolic fillet pitching moment also is more stable than other fillets pitching moment. In turn, the parabolic fillet generates a higher pitch-up and larger lift slope change after the vortex burst location moves over the wing. The diamond fillet lift coefficient is higher than

the linear fillet lift coefficient from 16° to 24° angle of attack. The linear fillet has a higher lift coefficient than the diamond fillet from 26° to 36° angle of attack. There is a similar crossover in drag between the diamond and linear fillets. The diamond fillet generates a smoother lift curve than the linear or parabolic fillet. Both the linear and diamond fillets generate similar pitching moment curves.

- $M = 0.30$

The 0.5% linear, diamond, and parabolic fillets are compared to the baseline model at Mach 0.30 in Figure 8. The parabolic fillet lift is higher than that generated by the diamond or linear fillets. However, $C_{L_{max}}$ decreases from 1.75 to 0.99 with increasing Mach number. Unlike the Mach 0.18 results, the linear fillet generates an equal or higher lift coefficient than the diamond fillet. The linear fillet does not change lift slope until an angle of attack of 18° ($C_L = 0.8$) in comparison to 14° at Mach 0.18. However, the lift slope change is abrupt. The linear fillet drag coefficient tracks the parabolic fillet up to a C_L of 0.8. The linear fillet pitching moment coefficient matches the parabolic fillets pitching moment up to $C_L = 0.8$. The Mach 0.3 parabolic fillet pitching moment is less stable than at Mach 0.18.

- $M = 0.50$

As shown in Figure 9 the parabolic fillet generates the most lift followed by the linear, diamond, and baseline configurations. Both the parabolic and linear fillets have a sharp lift loss after 18° angle of attack. The diamond fillet has the same lift curve shape as the baseline configuration up to an angle of attack of 20° with 2.9% greater lift at 18° . At 21° angle of attack the baseline model lift curve intersects the diamond fillet's lift curve. The parabolic and linear fillets have drag coefficient curves with sharp breaks similar to their lift curves. Data were not obtained beyond an angle of attack of 24° due to balance limits.

- $M = 0.70$

The Mach 0.70 data, Figure 10, is limited to 16° angle of attack due to balance limits. The parabolic fillet generates a higher lift slope, lower drag and pitching moment than the other fillets and the baseline configuration.

- Repeatability

The diamond fillet repeatability is similar to the baseline configuration. The linear fillet repeatability is presented in Figure 11. Two of the three linear fillet runs have good agreement; however, the second run shows a large discrepancy, displaying a lower lift and higher pitching moment from 12° to 18° angle of attack. A definitive cause for this discrepancy in the lift curves is unknown. Possible explanations are the existence of bi-stable vortex structures or of run-to-run model change inconsistencies.

- Inverted Model

Unexpected results were obtained when the model was inverted. As shown in Figure 12 the linear and diamond fillets did not increase lift a substantial amount when compared to the upright data. The lift coefficient of the inverted parabolic fillet is also lower than that found in the upright model. It is not known if the decrease in lift between the upright and inverted model orientations is caused by the balance fairing acting as a fuselage that decouples the port and starboard vortices, or whether the change in leading edge bevel shape affects the vortex sheet roll-up characteristics. Neither pneumatic or PSP data were available to allow further characterization of this flow.

Fillet Size Effects On Longitudinal Characteristics

The effect of fillet shape and size (0.5%, 1%, and 2.5%) on longitudinal characteristics are presented at Mach 0.18, 0.3, and 0.5

- Linear Fillet

The effect of the 0.5%, 1%, and 2.5% linear fillets on longitudinal force and moment characteristics at Mach 0.18, 0.3, and 0.5 are shown in Figures 13 through 15. Figure 13 shows a trend of increasing lift with increasing fillet size at Mach 0.18 and at angles of attack above 14° . Increasing fillet size does not have a large influence on lift at or above 30° angle of attack. Drag coefficient increases with increasing fillet size for

a given angle of attack; however, it decreases for a given C_L . The 0.5% and 1% linear fillets increase pitching moment instability slightly. There was a more pronounced instability increase with the 2.5% linear fillet. There is no clear correlation with increasing Mach. One fillet size will generate a higher lift coefficient within an angle of attack range at one Mach but behave differently at another Mach. As depicted in Figures 13 through 15 as Mach increases, fillet size effects diminish.

- Diamond Fillet

The effect of the 0.5%, 1%, and 2.5% diamond fillets on longitudinal force and moment characteristics at Mach 0.18, 0.3, and 0.5 are shown in Figures 16 through 18. The only clear effect of variation in diamond fillet size is at Mach 0.3 between 14° and 22° angle of attack: the 2.5% fillet generates the highest lift coefficient, and the 1% fillet has a higher C_L than the 0.5% fillet from 16° to 22° . Only the 2.5% fillet shows an appreciable increase of pitching moment instability.

- Parabolic Fillet

Longitudinal data for the parabolic fillets is presented in Figures 19 through 21 for Mach numbers 0.18, 0.3, and 0.5, respectively. Increasing fillet size from 0.5% to 1% creates discontinuities in the C_L , C_D , and C_M curves. The 0.5% and 1% fillets generally produce the same force and moment coefficients up to the first discontinuity. The angle of attack where the first C_L discontinuity occurs decreases with increasing fillet size. The parabolic fillet is prone to large roll dynamics. Vapor screen video shows the dynamics are caused by unstable (oscillatory) left/right vortex bursting. At some angles of attack, the left and right vortices burst in a fixed symmetric or asymmetric pattern. The maximum lift generated is significantly higher in comparison to the other fillets and the baseline configuration.

Fillet Flow Field Characteristics

Flow field characteristics will be discussed by presenting upper surface pressure distribution plots from the pneumatic tap data and PSP derived pressure maps images. Vapor screen images will also be used in conjunction with the pressure data. The data is presented at 8° , 12° , 16° , 20° , 22° , and 24° angle of attack. It is also limited to the 1% fillets and Mach 0.5.

- Linear Fillet

As illustrated in Figure 22 the linear fillet flow field is dominated by the strake, fillet, and wing vortices. The strake vortex is immediately entrained by the fillet vortex causing the pneumatic and PSP data to show the fillet and wing vortices as a wide footprint with two suction peaks. At 16° angle of attack, the vortices mutually interact with each other resulting in a single footprint. The vapor screen images show that with increasing angle of attack the strake, fillet, and wing vortices roll-up into a single vortex. The fillet vortex is entrained under the wing vortex while the fillet vortex entrains the strake vortex. The strake and fillet vortex cores rotate around the wing vortex core.

- Diamond Fillet

Four pairs of vortices dominate the diamond fillet flow field: one from the strake, two from the fillet, and one from the wing. The vortex structure at various model stations is presented in Figure 23. The two vortices emanating from the fillet rapidly roll up into a single vortex, consequently, the upper surface pressure plots only show three distinct footprints at low angles of attack. As shown in the pressure tap and PSP pressure maps data, the strake, fillet, and wing vortices start to show a single pressure footprint with two suction peaks at higher angles of attack. The PSP pressure maps show the left wing vortex bursting at 22° angle of attack and the strake vortex pressure footprints becoming asymmetric.

- Parabolic Fillet

The pneumatic, PSP, and vapor screen data in Figure 24 show the majority of the vorticity rolls up into a single pair of vortices (left and right). A single pressure peak also depicts this. The vapor screen images show one clear vortex pair for the majority of vortex trajectory. The synergistic effect of concentrating the vorticity into a single vortex creates large suction peaks. The combined strake/wing vortex ceases to follow the wing

leading edge and “tears off.”¹⁹ After the vortex tears, a new vortex is formed along the wing leading edge. Asymmetric vortex bursting is clearly shown in the PSP data at 20° and 22° angles of attack.

SUMMARY AND CONCLUSIONS

A 76°/40° sweep double delta wing was tested in the NASA Langley 7x10 ft HST from Mach 0.18 to 0.7 and from -4° to 42° angle of attack. The double delta wing strake/wing juncture was modified from the baseline configuration with three fillet shapes: linear, diamond, and parabolic. Fillet size was also varied. The linear and diamond fillets with total (left plus right) additional fillet area to wing planform area of 0.5%, 1%, and 2.5% were tested, while parabolic fillet varied 0.5% and 1%.

It was found that with increasing Mach number the baseline configuration lift increased while drag decreased. Since the wind tunnel Reynolds number varied with atmospheric conditions and Mach number, Reynolds number effects cannot be separated from Mach effects. Pitching moment coefficient did not vary below Mach 0.5 and a C_L of 0.6. At Mach 0.7 pitching moment was more stable. Above a C_L of 0.6 there is no clear Mach number trend. The baseline lift curves can be characterized by three distinct regions: The first is an angle of attack range of approximately -4° to 12° where the lift slope gradually increases. In this range, the wing vortex does not entrain and mix with the strake vortex. The second region is from approximately 12° to 32° angle of attack, where the lift curve is characterized by a break and reduction in lift slope. In this angle of attack range, the wing vortex entrains the strake vortex, the vortex burst point of the combined vortices moving upstream with increasing angle of attack. The third region occurs post-stall, after 36° angle of attack, where lift slope is negative. Under these conditions the strake vortex burst point is near the strake apex. Increasing Mach delays the entrainment of the strake vortex by the wing vortex.

Baseline configuration PSP pressure map images at Mach 0.7 clearly show striations on the strake vortex footprint. The striation color indicates regions of local high pressure. The striation pattern has the wrong orientation to be the high and low suction peaks associated with the shear layer instability roll up shown in Reference 12 (Figure 16) and in Reference 32 (Figures 3.22 and 3.23). As depicted in References 5 through 16 the near surface flow under a swept leading edge generated vortex proceeds in a downstream and spanwise outboard direction. The striations observed here are perpendicular to the near surface flow under the vortex, supporting the hypothesis that the striations are caused by localized shock waves and subsequent pressure recovery. The striations are not seen in the wing vortex.

All the fillets increase lift from approximately 8° to 32° angle of attack. The parabolic fillet generates the most lift, while the linear and diamond fillets increase lift to a varying degree at different angles of attack. Drag decreases with increasing fillet size. Pitching moment does not significantly vary with the linear and diamond fillets. The parabolic fillet increases pitch stability at low angles of attack and pitch-up at elevated angles of attack. Increasing fillet size typically increases lift and pitch stability, and reduces drag. However, increasing parabolic fillet size also increases the number of lift curve breaks and lowers the angles of attack where they occur.

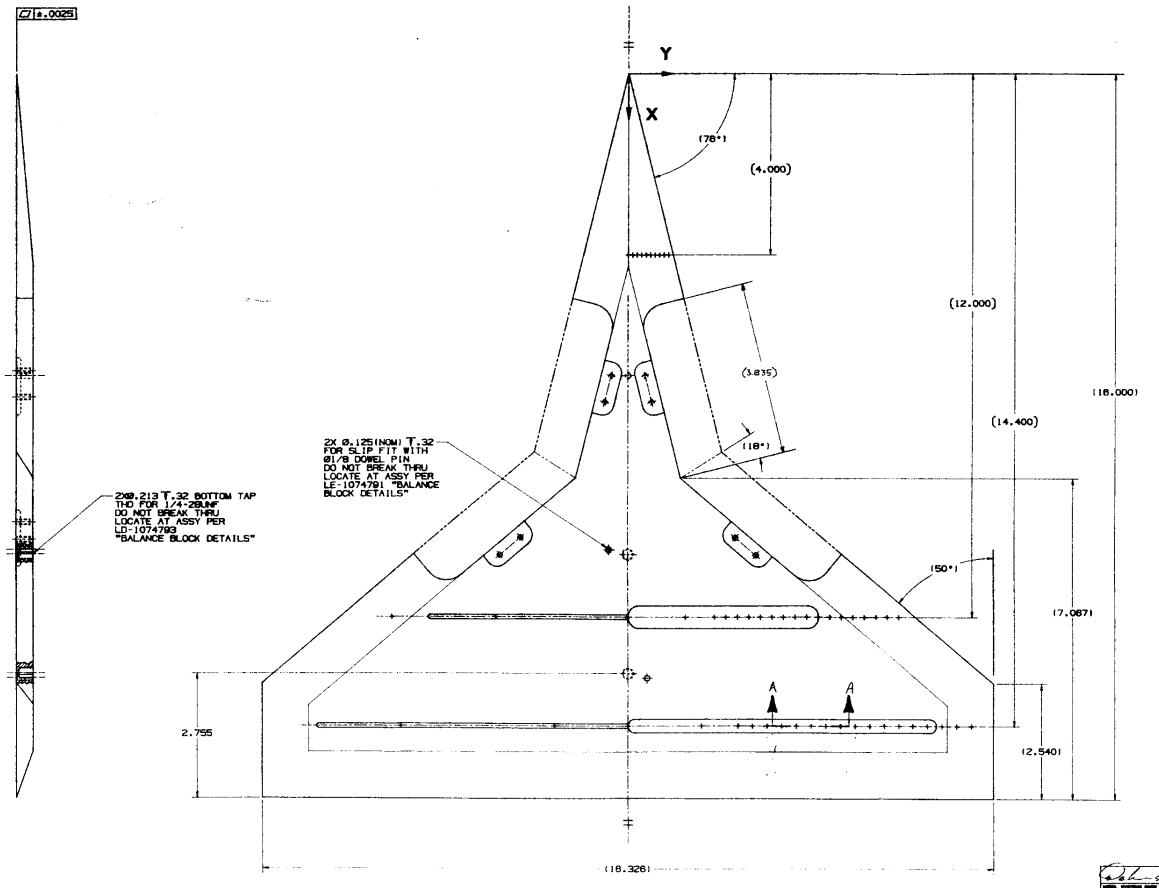
The fillet effects decrease with increasing Mach number. It is hypothesized this is caused by a delay of the strake vortex entrainment by the wing vortex. A similar delay between strake and wing vortex interactions is observed in the baseline configuration.

The fillets tested show potential of improving aircraft aerodynamic performance. However, further research needs to be conducted on the Reynolds number, center body (fuselage), and leading-edge shape effects on fillet effectiveness.

REFERENCES

1. Dhah, G.H., Grafton, S.B., Guynn, M.D., Brandon, J.M., Dansberry, B.E., and Patel, S.R., "Effect of Vortex Flow Characteristics on Tail Buffet and High Angle-of-Attack Aerodynamics of a Twin-Tail Fighter Configuration," High-Angle-of-Attack Technology Conf., NASA LARC, Hampton, VA, November 1990.
2. Lan, Edward C. and Lee, I.G., "Investigation of Empennage Buffeting," NASA CR-179426, January, 1987.
3. Hummel, D., "On the Vortex Formation Over a Slender Wing at Large Incidence," AGARD-CP-247, 1979.
4. Barlett, G.E. and Vidal, R.J., "Experimental Investigation Influence of Edge Shape on the Aerodynamic Characteristics of Low Aspect Ratio Wings at Low Speeds," J. of the Aeronautical Sciences, "Vol. 22, No. 8, Aug. 1955.
5. Erickson, G.E., "Vortex Flow Correlation," AFWAL, TR-80-3143, January 1981.
6. O'Neil, P.J., Roos, F.W., Kegelmann, J.T., Barnett, R.M., and Hawk, J.D., "Investigation of Flow Characteristics of a Developed Vortex," NADC-89114-60, May 1989.
7. Cunningham, A.M., Jr. and den Boer, R.G., "Unsteady Low Speed Wind Tunnel Test of a Straked Delta Wing, Oscillating in Pitch," AFWALTR-873098, Pts. I-VI, 1987.
8. Brennenstuhl, U., and Hummel, D., "Vortex Formation Over Double-Delta Wings," ICAS-82-6.6.3, 1982.
9. Olsen, P.E., and Nelson, R.C., "Vortex Interaction Over Double-Delta Wings at High Angle of Attack," AIAA Paper 89-2191-CP, 1989.
10. Verhaagert, N.G., "An Experimental Investigation of the Vortex Flow Over Delta and Double-Delta Wings at Low Speed," Delft University of Technology, Report LR-372, September 1983.
11. Thompson, D.H., "Visualization of Vortex Flows Around Wings with Highly Swept Leading Edges," 9th Australian Fluid Mechanics Conference, Auckland, December 1986.
12. Erickson, G.E., "Wind Tunnel Investigation of the Intersection and Breakdown Characteristics of Slender-Wing Vortices at Subsonic, Transonic, and Supersonic Speeds," NASA TP 3114, November 1991.
13. Erickson, G.E., "Wind Tunnel Investigation of Vortex Flows on F/A-18 Configuration at Subsonic Through Transonic Speeds," NASA TP 3111, December 1991.
14. Kern, S.B., "A Numerical Investigation of Vortex Flow Control Through Small Geometry Modifications at the Strake/Wing Junction of a Cropped Double Delta Wing," AIAA Journal of Aircraft, Vol. 30, No. 6, Nov-Dec 1993, pp. 818-825.
15. Kern, S.B., "Investigation of Vortex Flow Control Using Fillets at the Strake/Wing Junction of a Double Delta Wing," Master of Science Thesis, Pennsylvania State University, May 1992.
16. Ekaterinaris, J.A., et al, "Numerical Investigation of the Flow Over a Double Delta Wing at High Incidence," AIAA-91-0753, Reno, Nevada, January 1991.
17. Hensch, M.J., Luckring J.M., "Connection Between Leading-Edge Sweep, Vortex Lift, and Vortex Strength for Delta Wings," AIAA Journal of Aircraft, Vol. 27, No. 5, May 1990.
18. Lamar, J.E., "Nonlinear Lift Control at High Speed and High Angle of Attack using Vortex Flow Technology," AGARD, 1986.
19. Rao D.M., "Vortical Flow Management for improved Configuration Aerodynamics – Recent Experiences," Paper No. 30, AGARD Symposium on Aerodynamics of Vortical Type Flows in Three Dimensions, Rotterdam, Netherlands, April 1983.

20. Rao, D.M. and Campbell, J.F., "Vortical Flow Management Techniques," Progress in Aerospace Sciences, Volume 24, pp. 173-224, 1987.
21. Bobbitt, P.J. and Foughner, J.E., "Pivotable Strakes for High Angle of Attack Control," SAE Paper No. 851821, October 1985.
22. Malcolm, G.N., Lewis, L.C., and Ng, T.T., "Development of Non-Conventional Control Methods for High-Angle-of-Attack Flight using Vortex Manipulation," WL-TR-913041, June 1991.
23. Straka, W.A., "Effects of Wing Planform Shaping on Leading-Edge Vortex Breakdown Characteristics," Master Thesis, George Washington University, September 1991.
24. McLachlan, B.G., and Bell, J.H., "Pressure-Sensitive Paint in Aerodynamic Testing," Experimental Thermal and Fluid Science, Vol. 10, pp.470-485, 1995
25. Alkhozan, A. M., "Interaction, Bursting and Control of Vortices of a Cropped Double-Delta Wing at High Angle of Attack," Thesis Naval Postgraduate School, March 1994.
26. McLachlan, B.G., Bell, JH, et. al., "Pressure Sensitive Paint Use in the Supersonic High-Sweep Oblique Wing (SHOW) Test," AIAA 92-2686, June 1992.
27. Bell, J.H., and McLachlan B.G., "Image Registration for Luminescent Paint Sensors," AIAA 93-0178, January 1993.
28. Erickson, G.E., and Inenaga, A.S., "Fiber Optic-Based Laser Vapor Screen Flow Visualization for Aerodynamic Research in Larger-Scale Subsonic and Transonic Tunnels," 6th International Flow Visualization Symposium, 4-9 October 1992, Yokohama, Japan.
29. Fox, C.H. Jr., and Huffman, J.K., "Calibration and Test Capabilities of the Langley 7- by 10- High Speed Tunnel," NASA TM X-74027, May 1977.
30. Herriot, J.H., "Blockage Corrections for Three-Dimensional-Flow Closed-Throat Wind Tunnels, with Consideration of the Effect of Compressibility," NACA Report 995, 1950
31. Gillis, C.L., Polhamus, E.C., and Gray J.L., "Charts for Determining Jet-Boundary Corrections for Complete Models in 7- by 10-Foot Closed Rectangular Wind Tunnels," NACA ARR No. L5G31 or WR L-123, September 1945.
32. Campbell, J.F., and Chambers, J.R. "Patterns in the Sky-Natural Visualization of Aircraft Flow Fields," NASA SP-514, 1994.



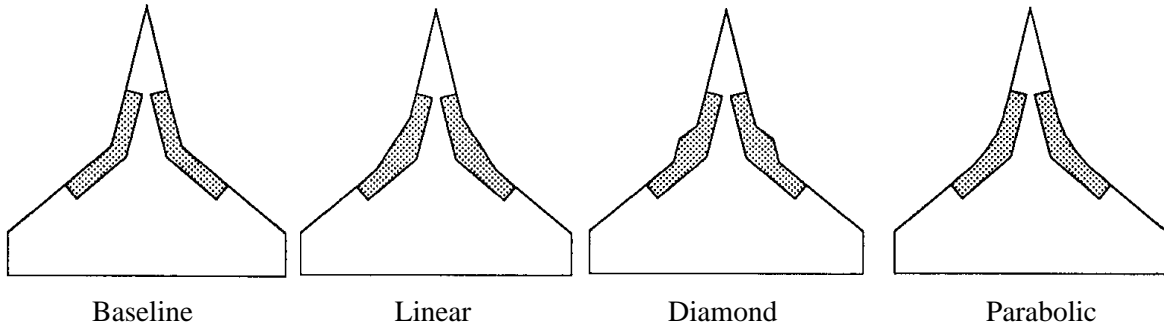


Figure 2- Baseline model and fillet configurations

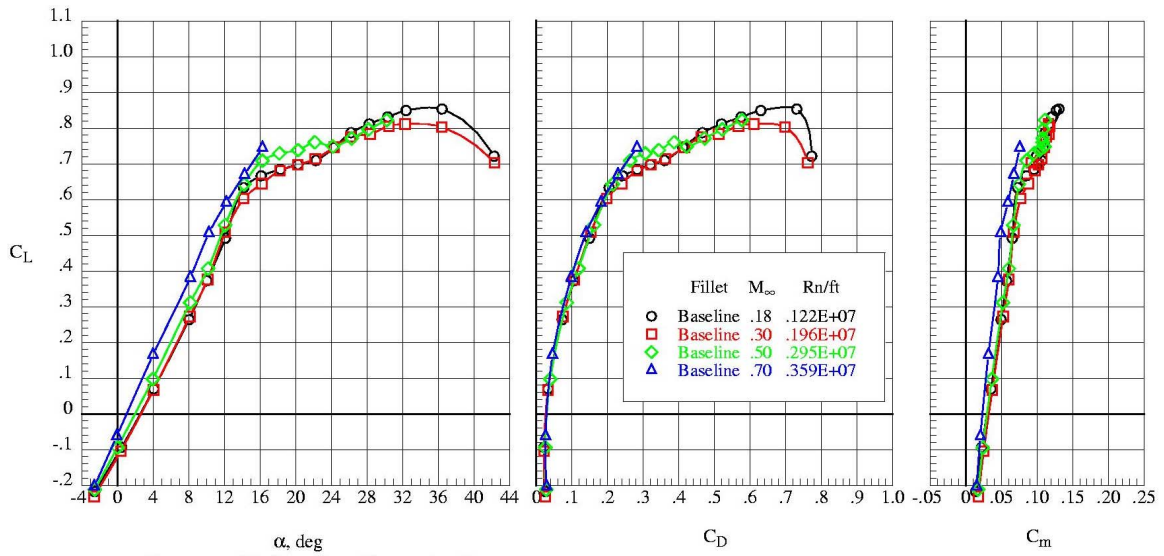


Figure 3- Mach Effects on Baseline Configuration Longitudinal Characteristics

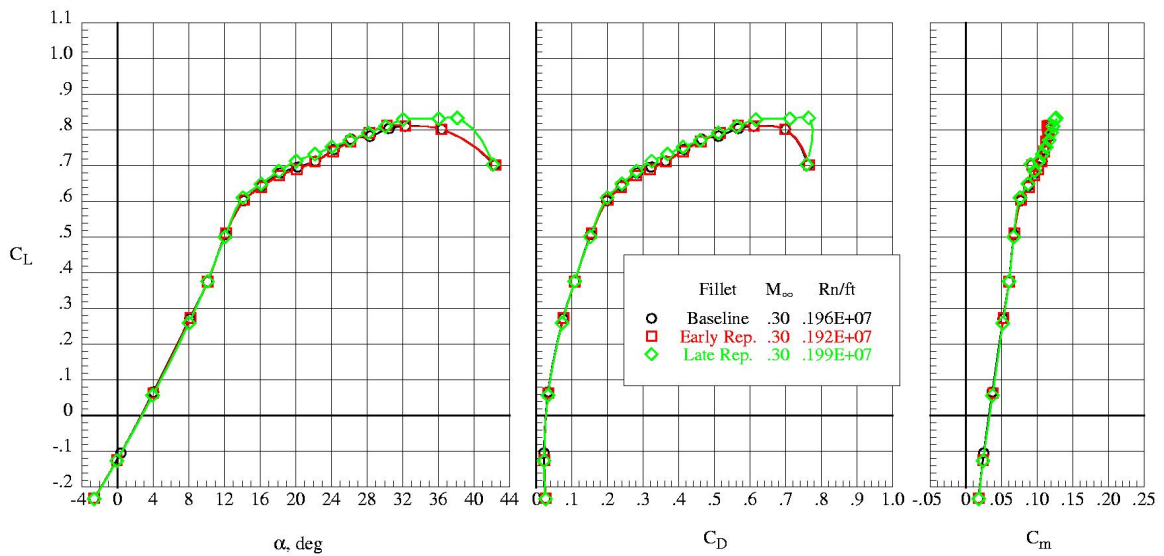


Figure 4- Repeatability of Baseline Configuration Longitudinal Characteristics, Mach 0.3

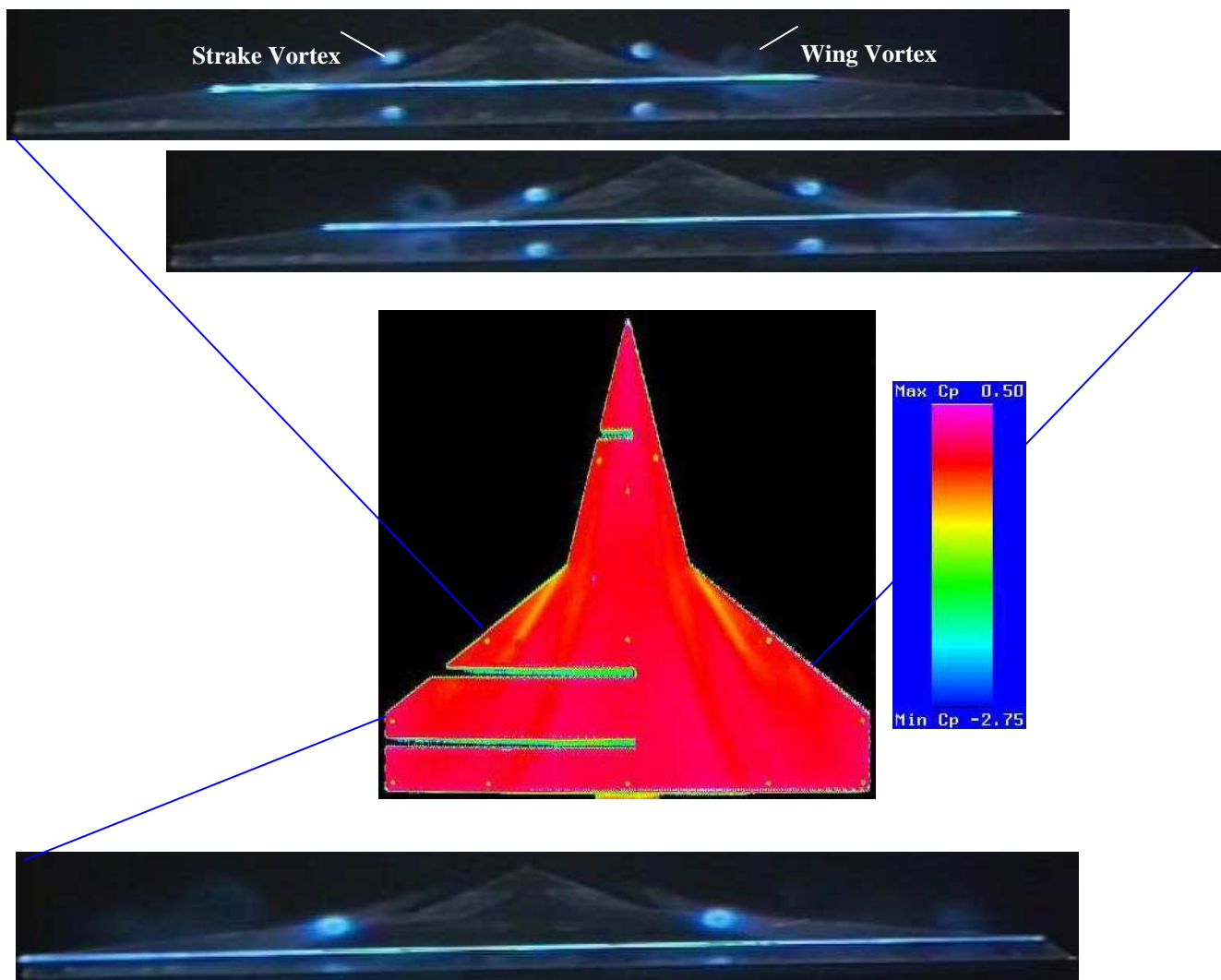
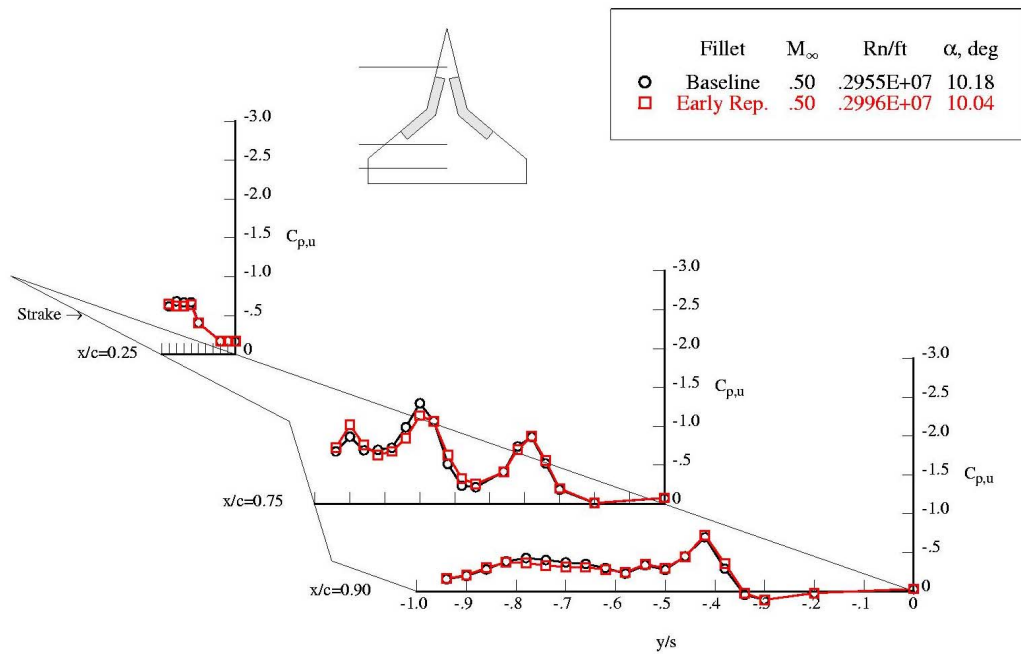


Figure 5- Baseline Configuration Flow Field and Pressure Distribution, Mach 0.5, AOA 10°

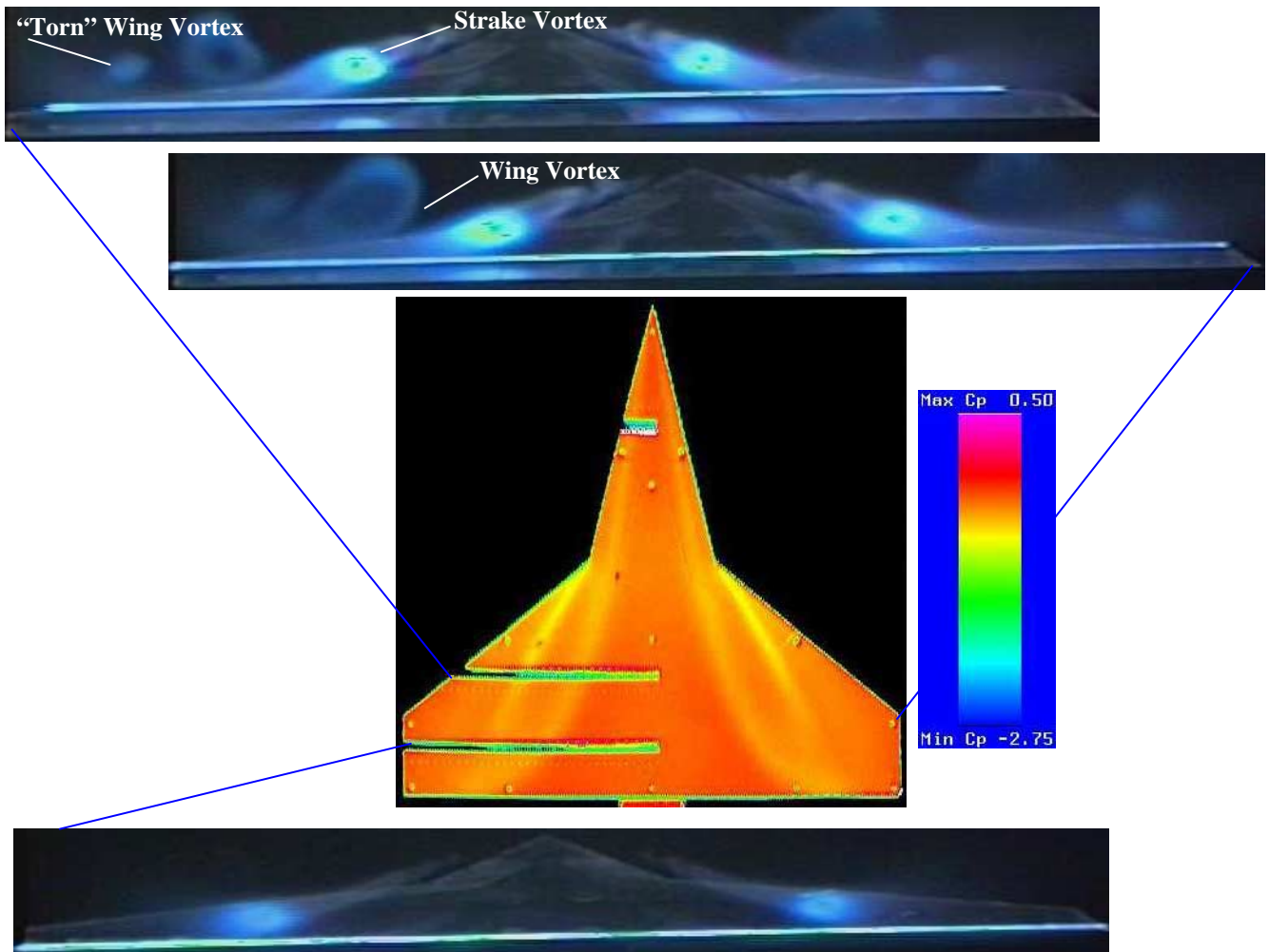
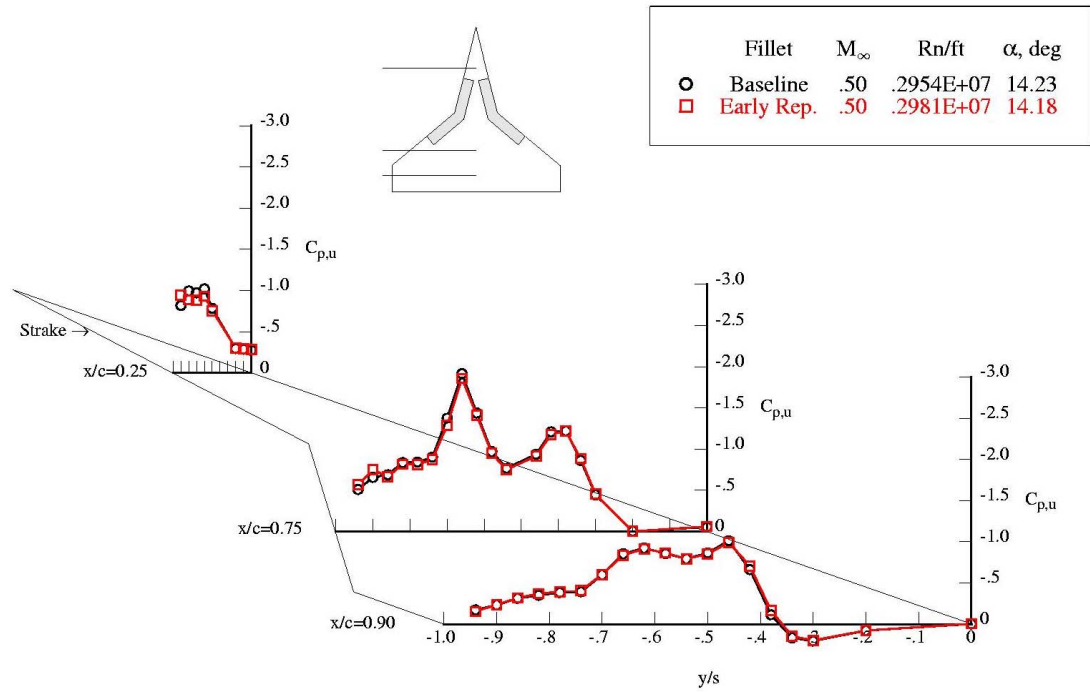


Figure 5 (cont.)- Baseline Configuration Flow Field and Pressure Distribution, Mach 0.5, AOA 14°

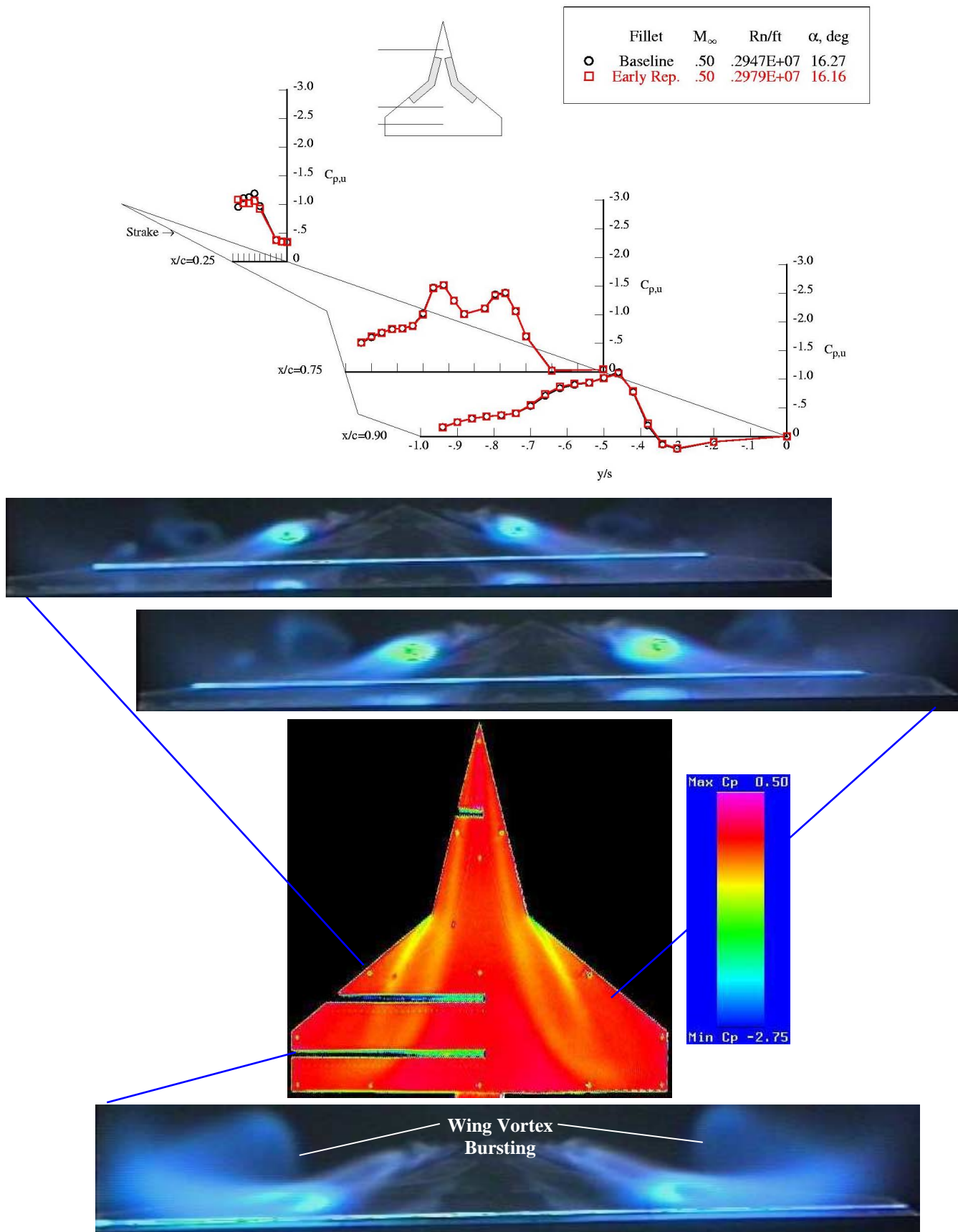


Figure 5 (cont.)- Baseline Configuration Flow Field and Pressure Distribution, Mach 0.5, AOA 16°

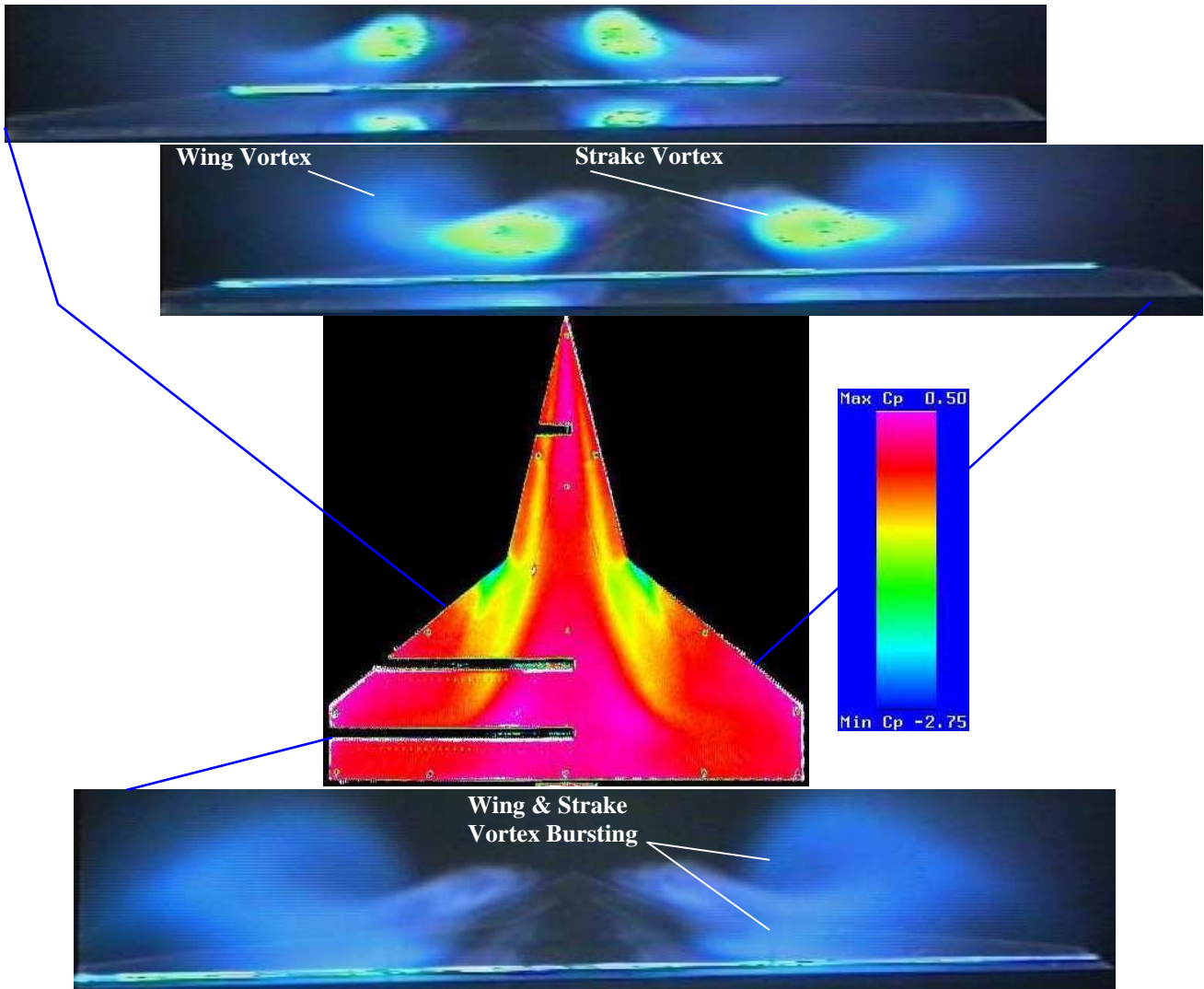
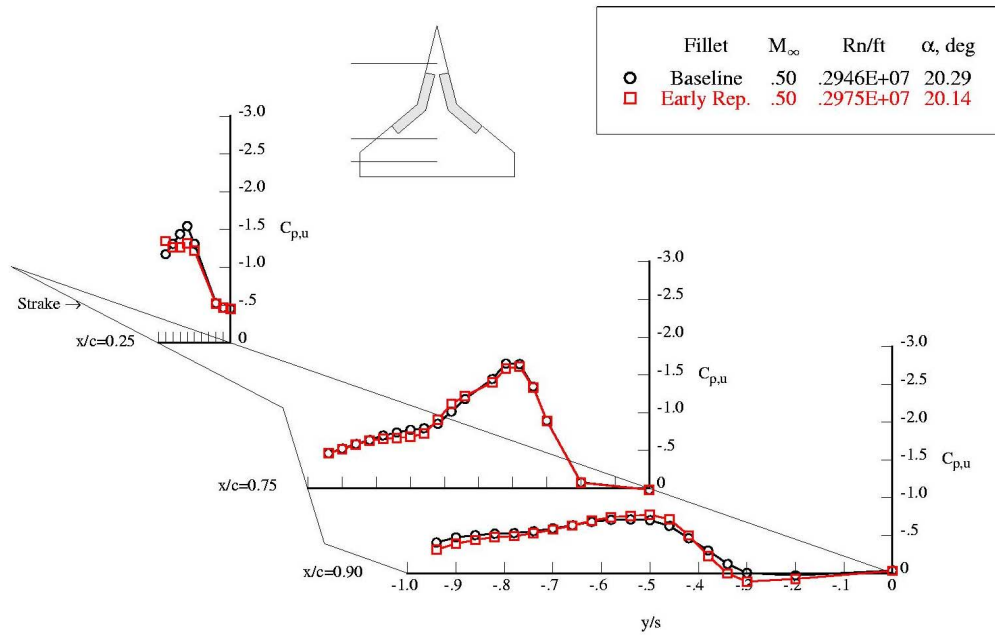


Figure 5 (cont.)- Baseline Configuration Flow Field and Pressure Distribution, Mach 0.5, AOA 20°

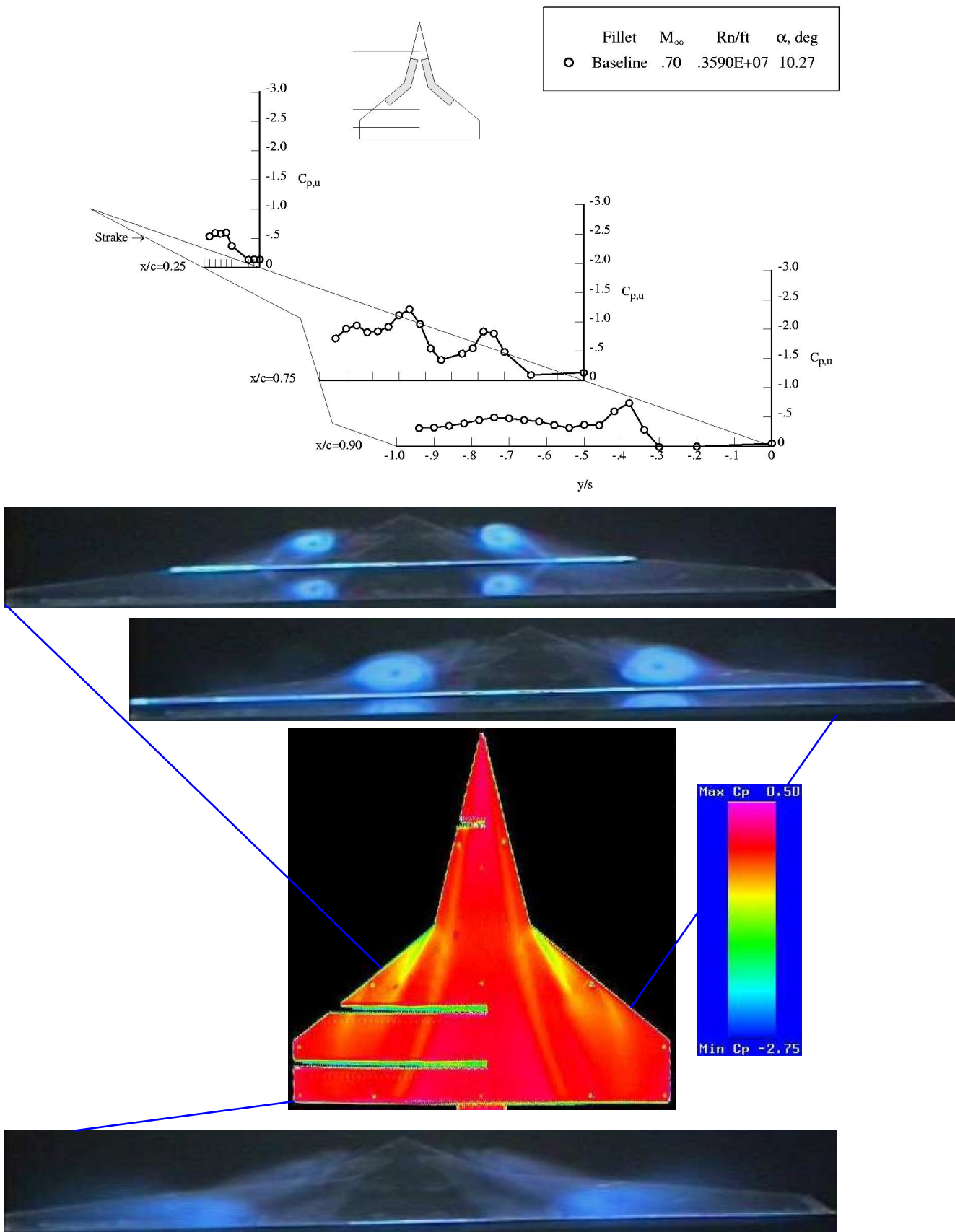


Figure 6- Baseline Configuration Flow Field and Pressure Distribution, Mach 0.7, AOA 10°

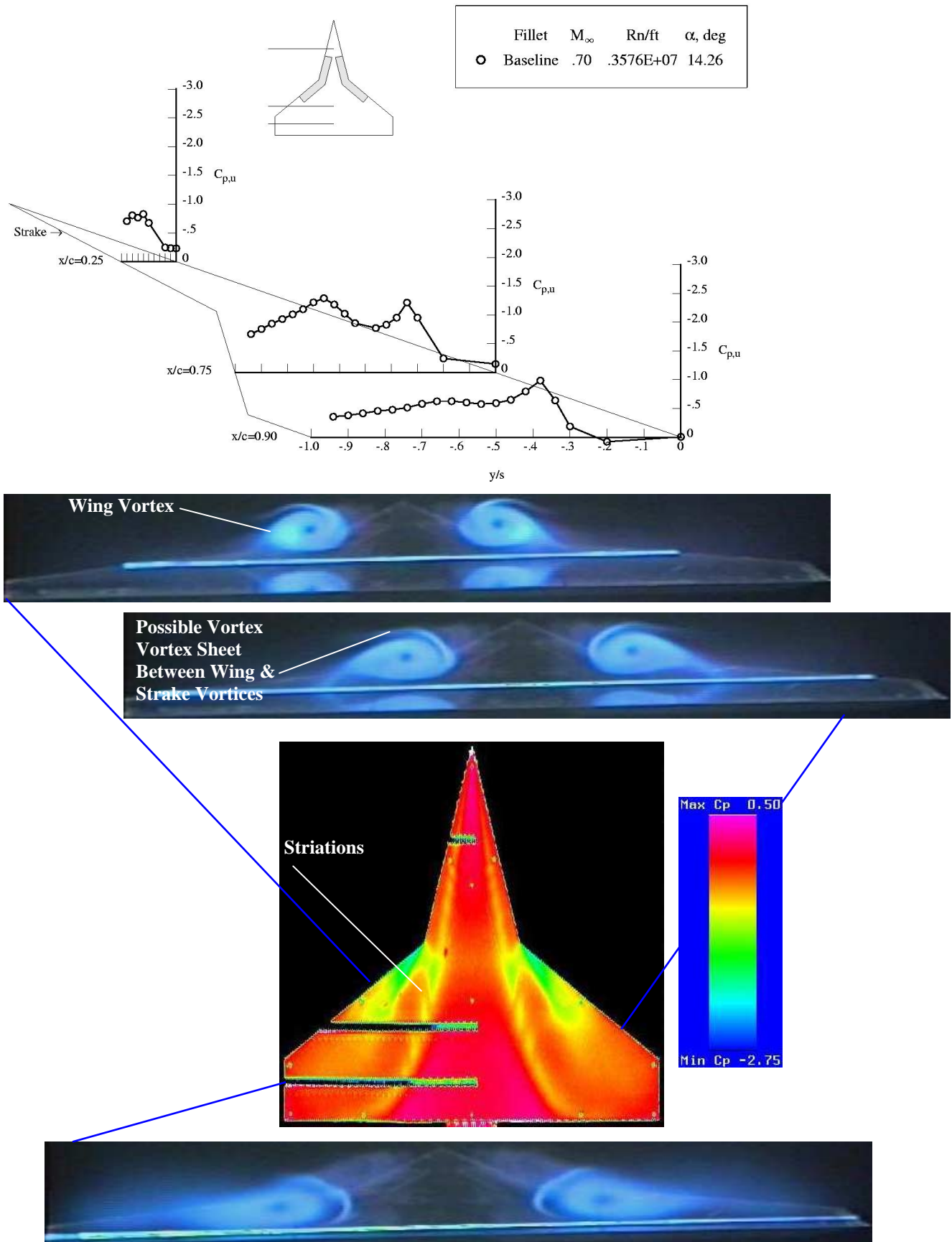


Figure 6 (cont.)- Baseline Configuration Flow Field and Pressure Distribution, Mach 0.7, AOA 14°

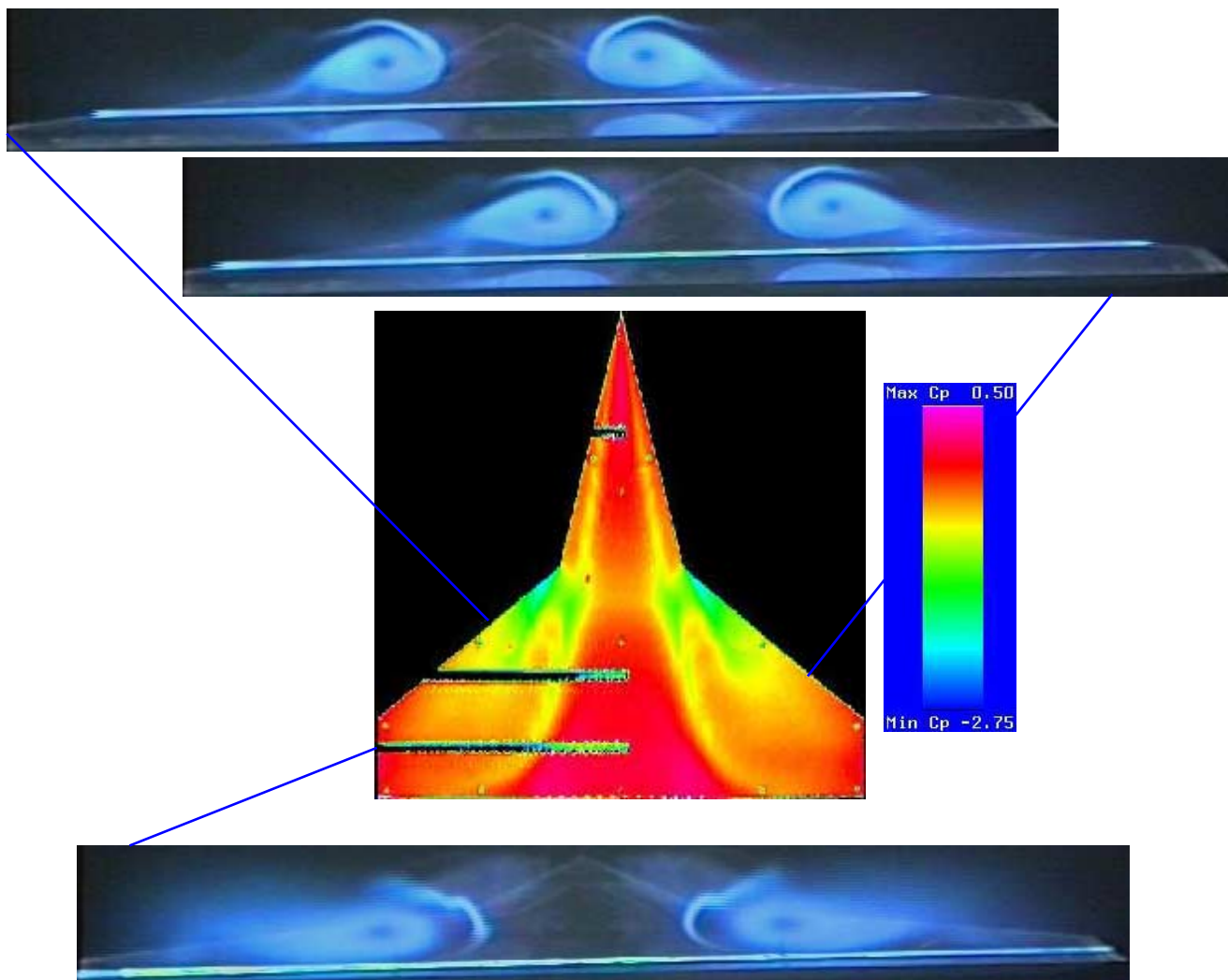
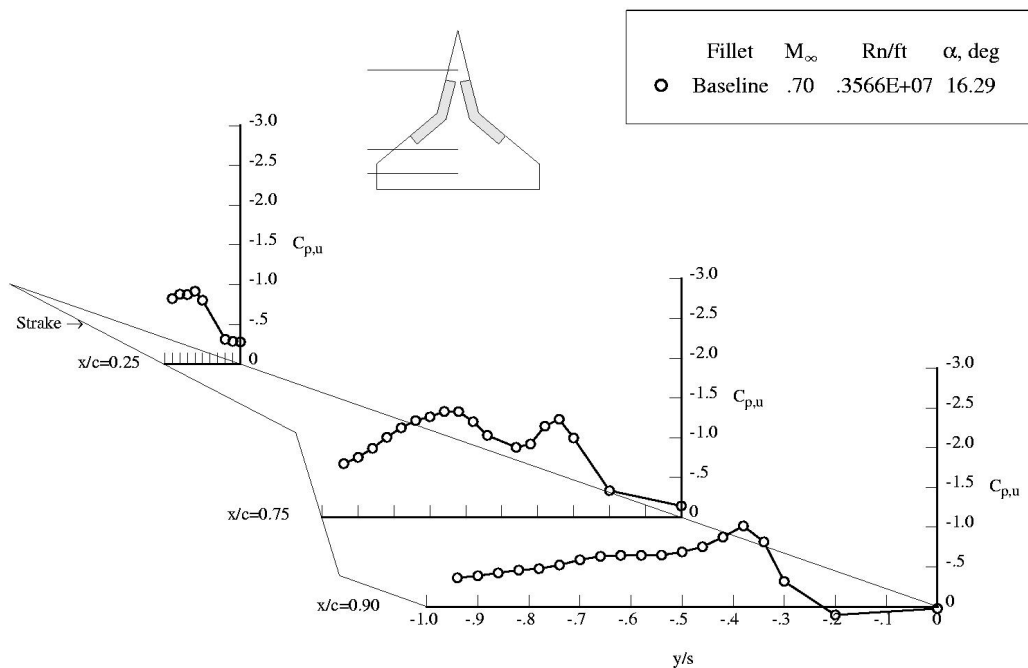


Figure 6 (cont.)- Baseline Configuration Flow Field and Pressure Distribution, Mach 0.7, AOA 16°

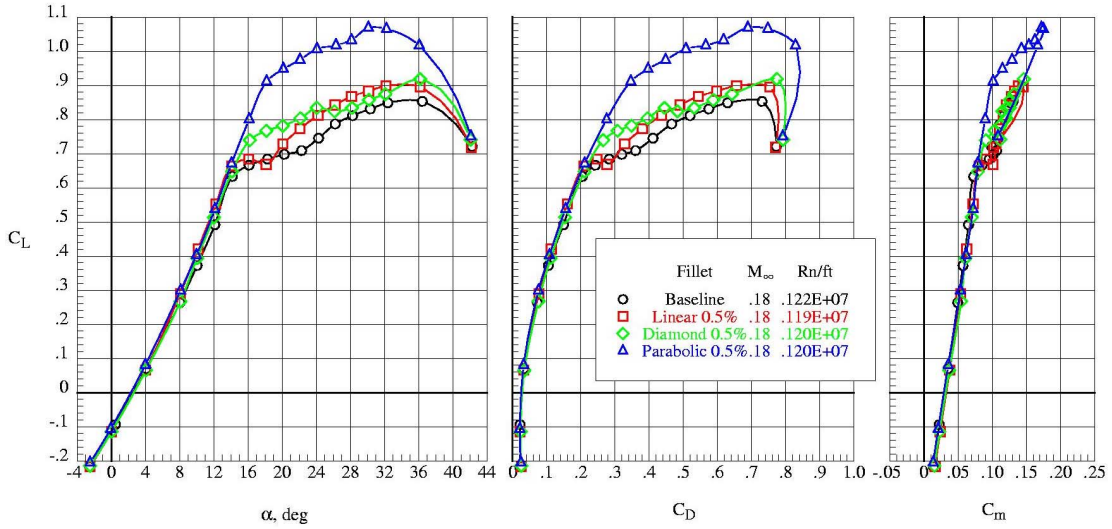


Figure 7- 0.5% Fillet Effect on Longitudinal Characteristics, Mach 0.18

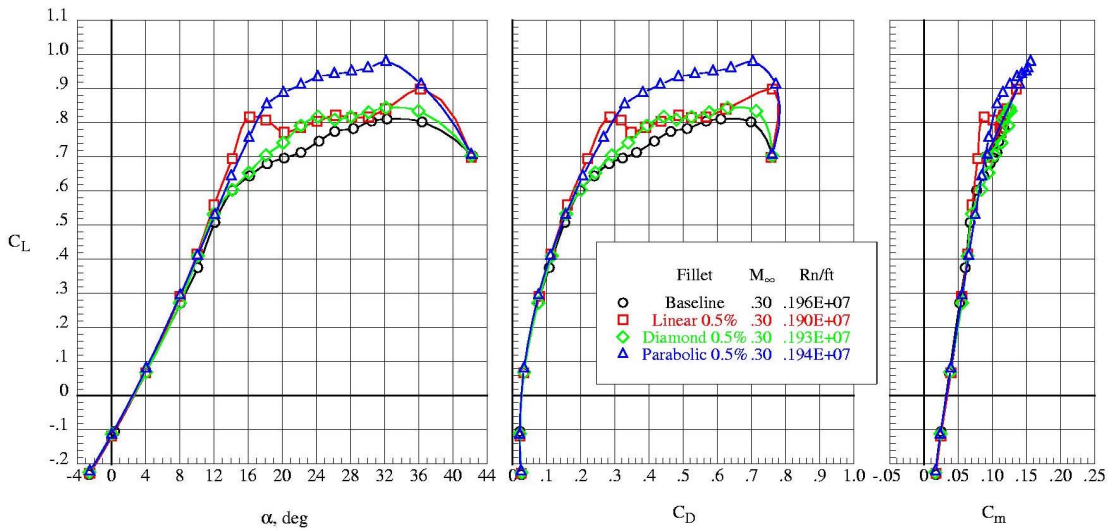


Figure 8- 0.5% Fillet Effect on Longitudinal Characteristics, Mach 0.3

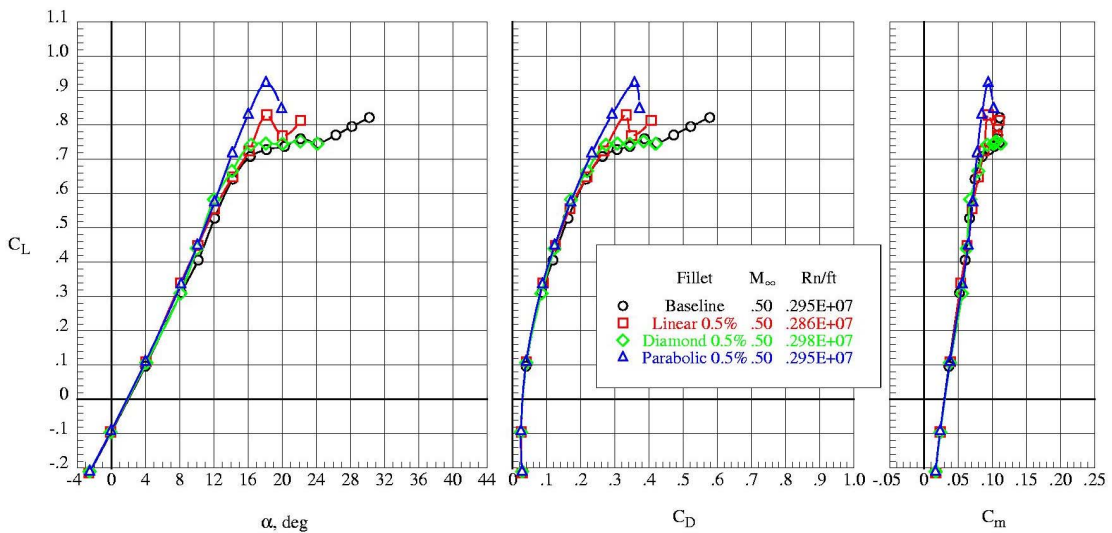


Figure 9- 0.5% Fillet Effect on Longitudinal Characteristics, Mach 0.5

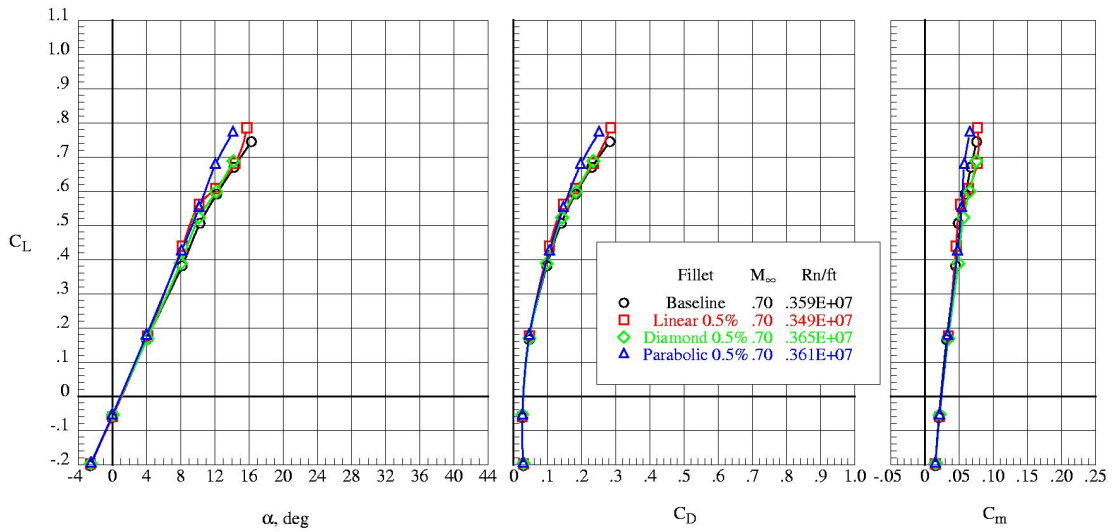


Figure 10- 0.5% Fillet Effect on Longitudinal Characteristics, Mach 0.7

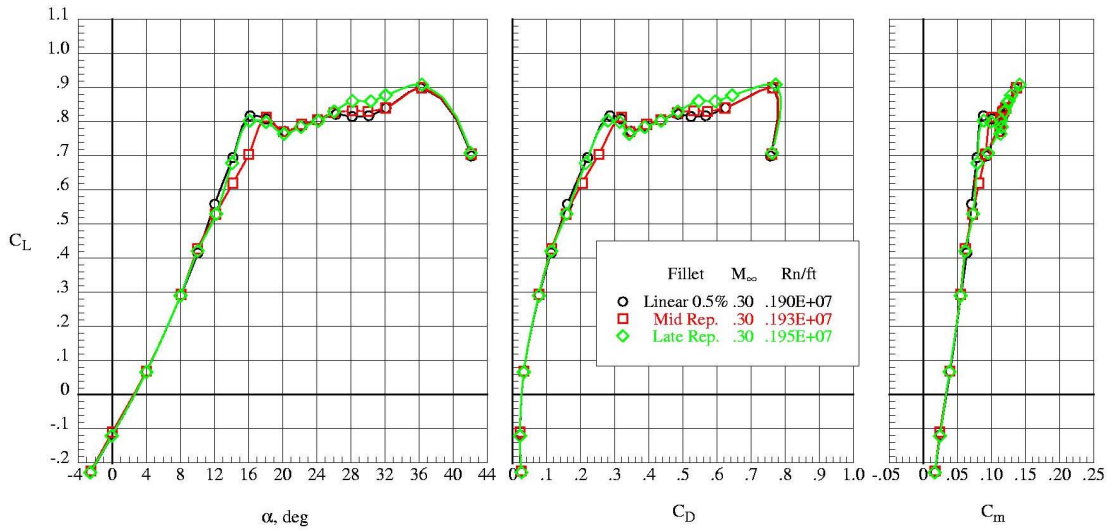


Figure 11- 1% Linear Fillet Repeatability, Mach 0.3

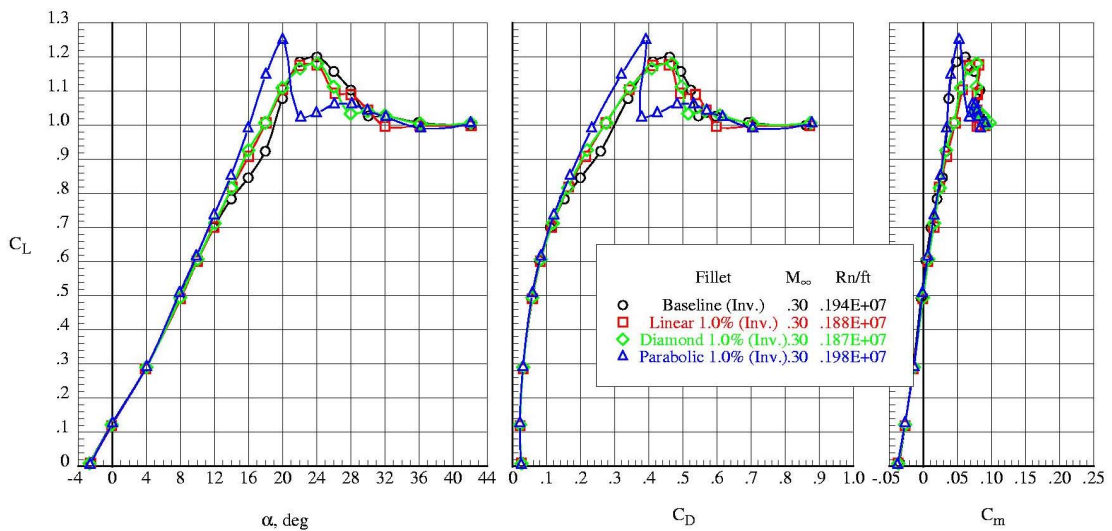


Figure 12- Fillet Effects On Inverted Model, Mach 0.3

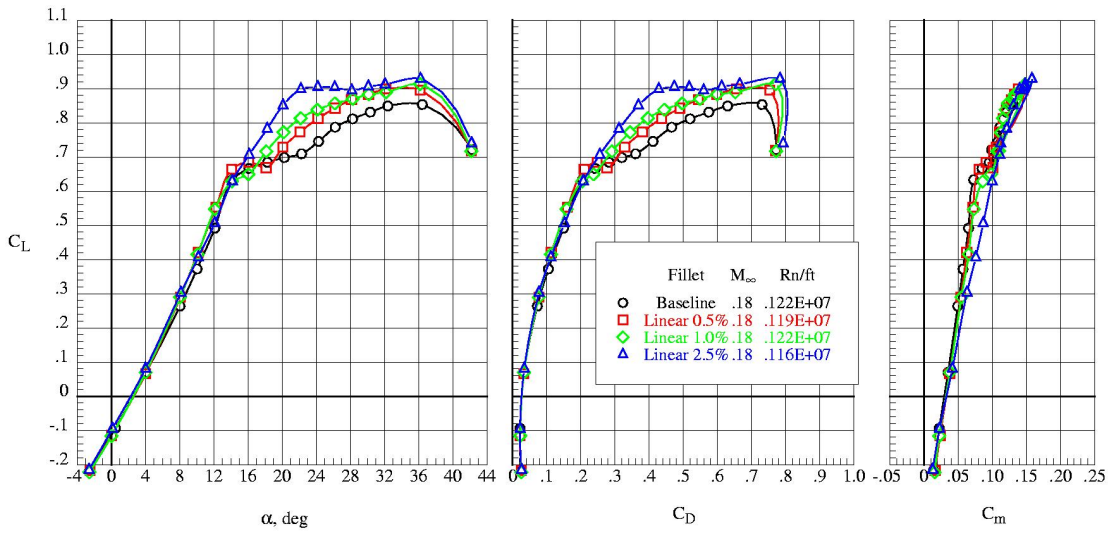


Figure 13- Linear Fillet Size Effect on Longitudinal Characteristics, Mach 0.18

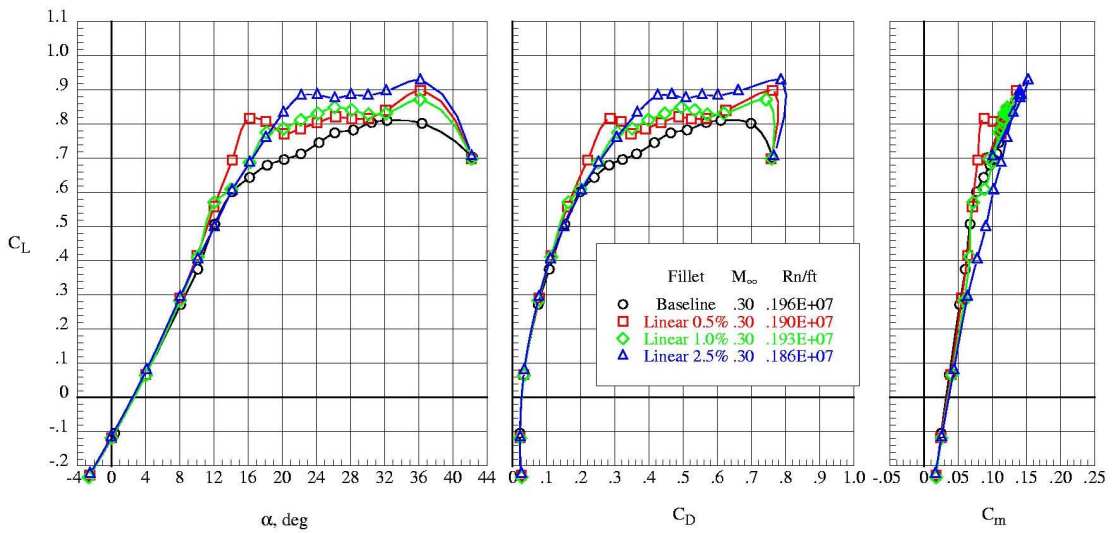


Figure 14- Linear Fillet Size Effect on Longitudinal Characteristics, Mach 0.3

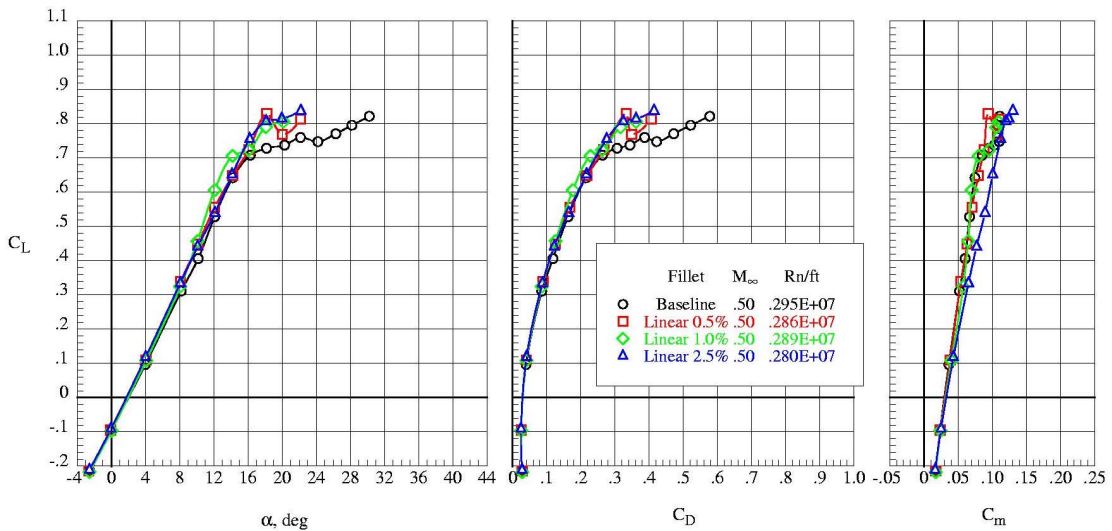


Figure 15- Linear Fillet Size Effect on Longitudinal Characteristics, Mach 0.5

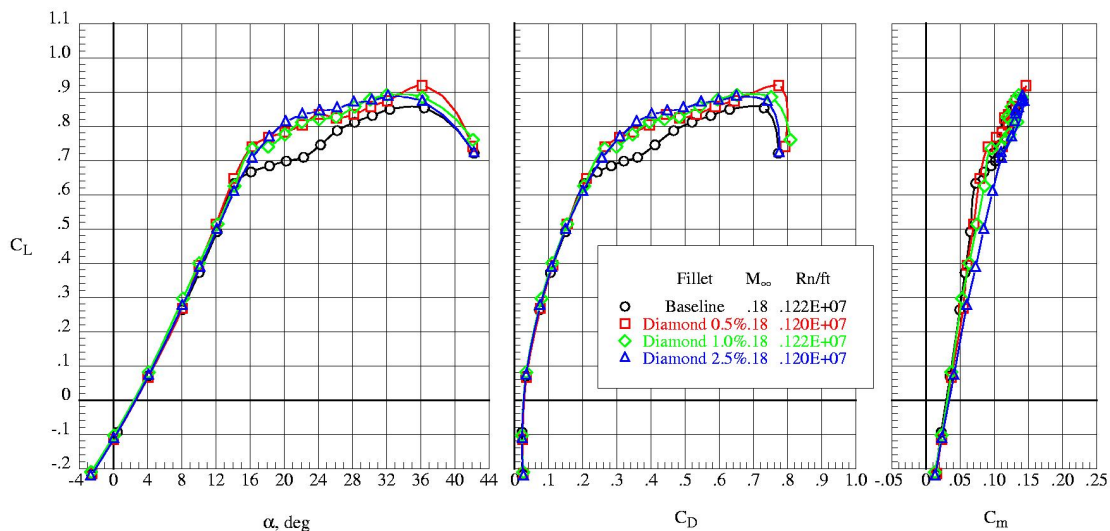


Figure 16- Diamond Fillet Size Effect on Longitudinal Characteristics, Mach 0.18

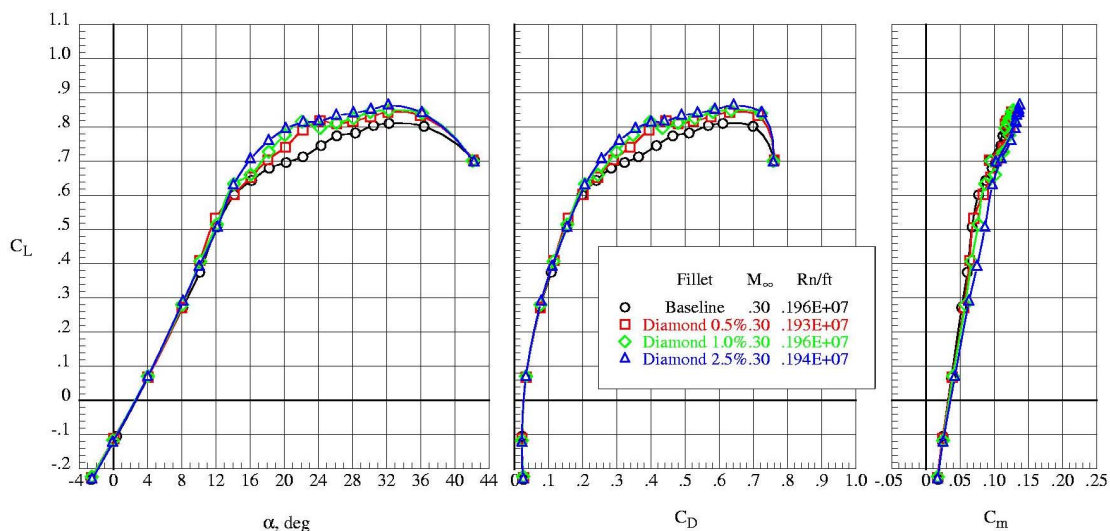


Figure 17- Diamond Fillet Size Effect on Longitudinal Characteristics, Mach 0.3

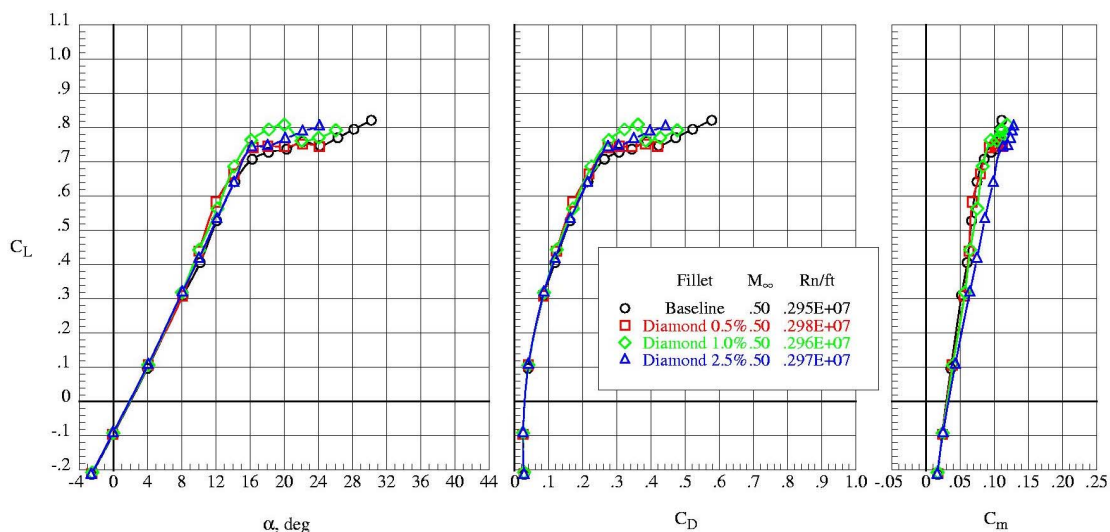


Figure 18- Diamond Fillet Size Effect on Longitudinal Characteristics, Mach 0.5

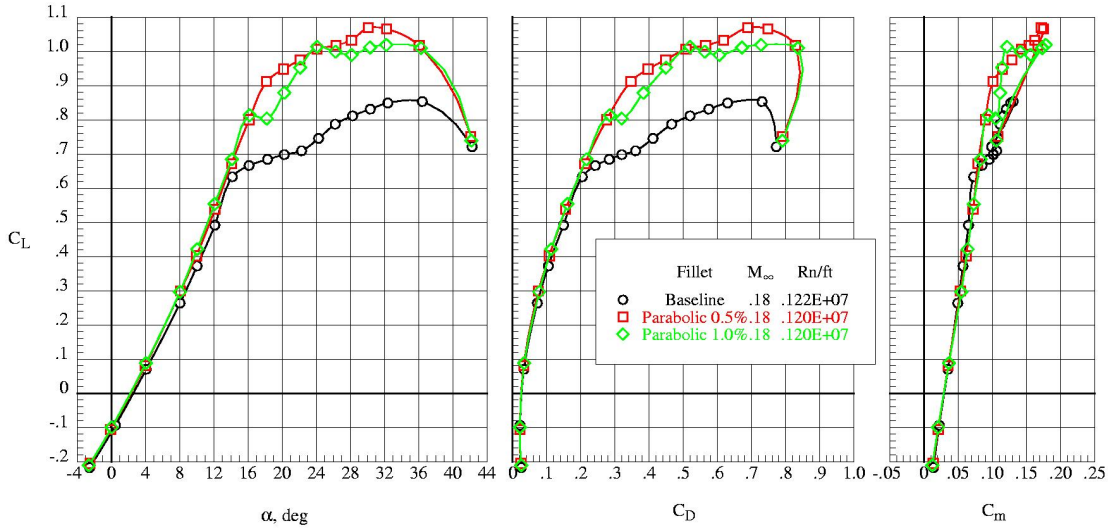


Figure 19- Parabolic Fillet Size Effect on Longitudinal Characteristics, Mach 0.18

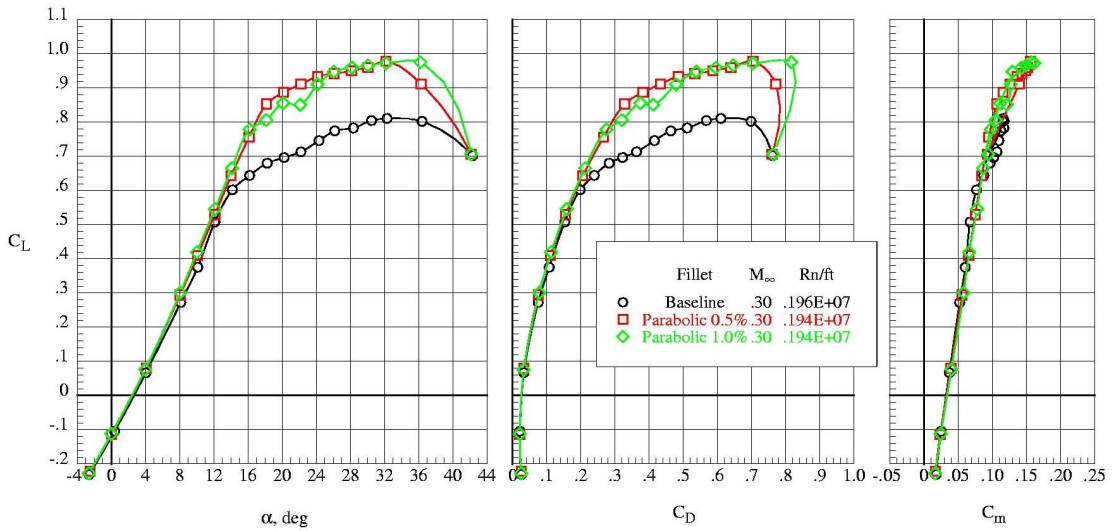


Figure 20- Parabolic Fillet Size Effect on Longitudinal Characteristics, Mach 0.3

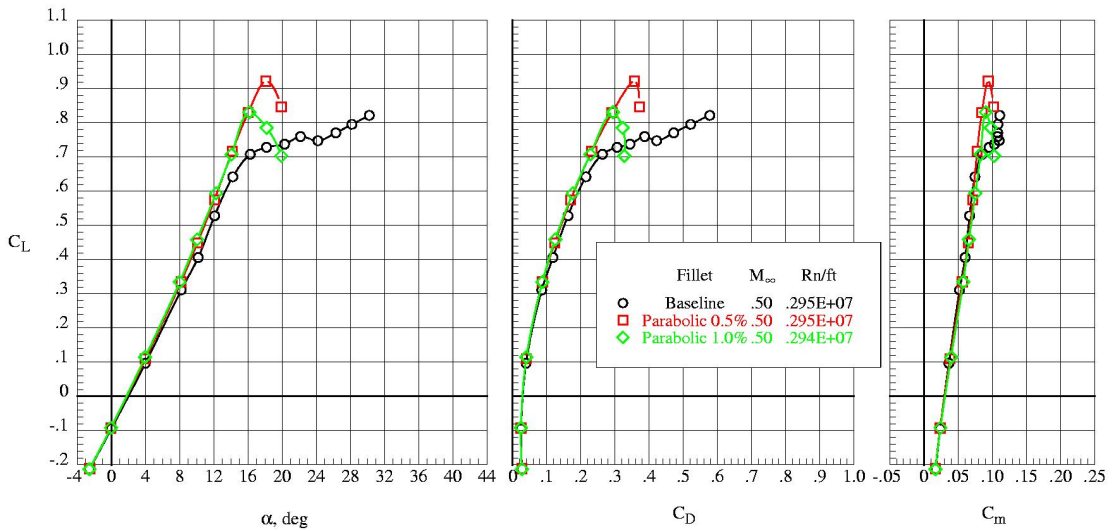


Figure 21- Parabolic Fillet Size Effect on Longitudinal Characteristics, Mach 0.5

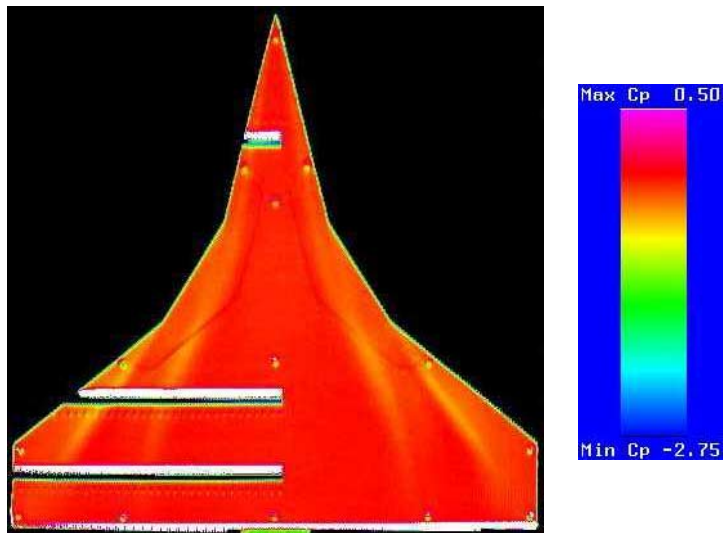
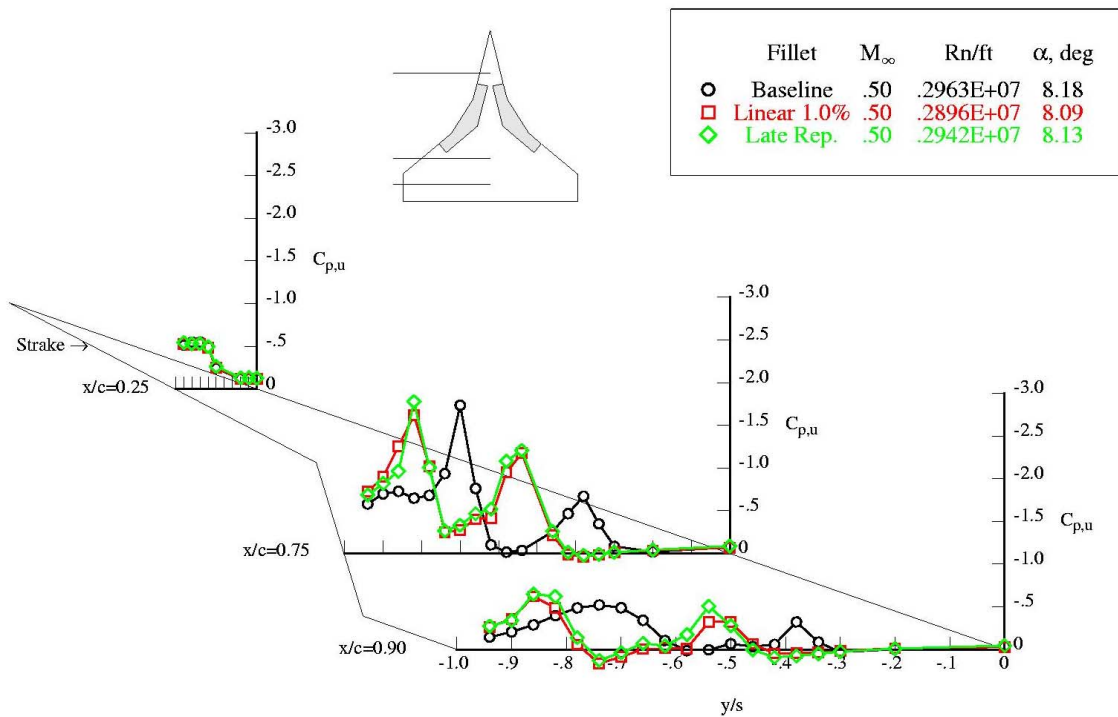


Figure 22- Linear Fillet Flow Field and Pressure Distribution, Mach 0.5, AOA 8°

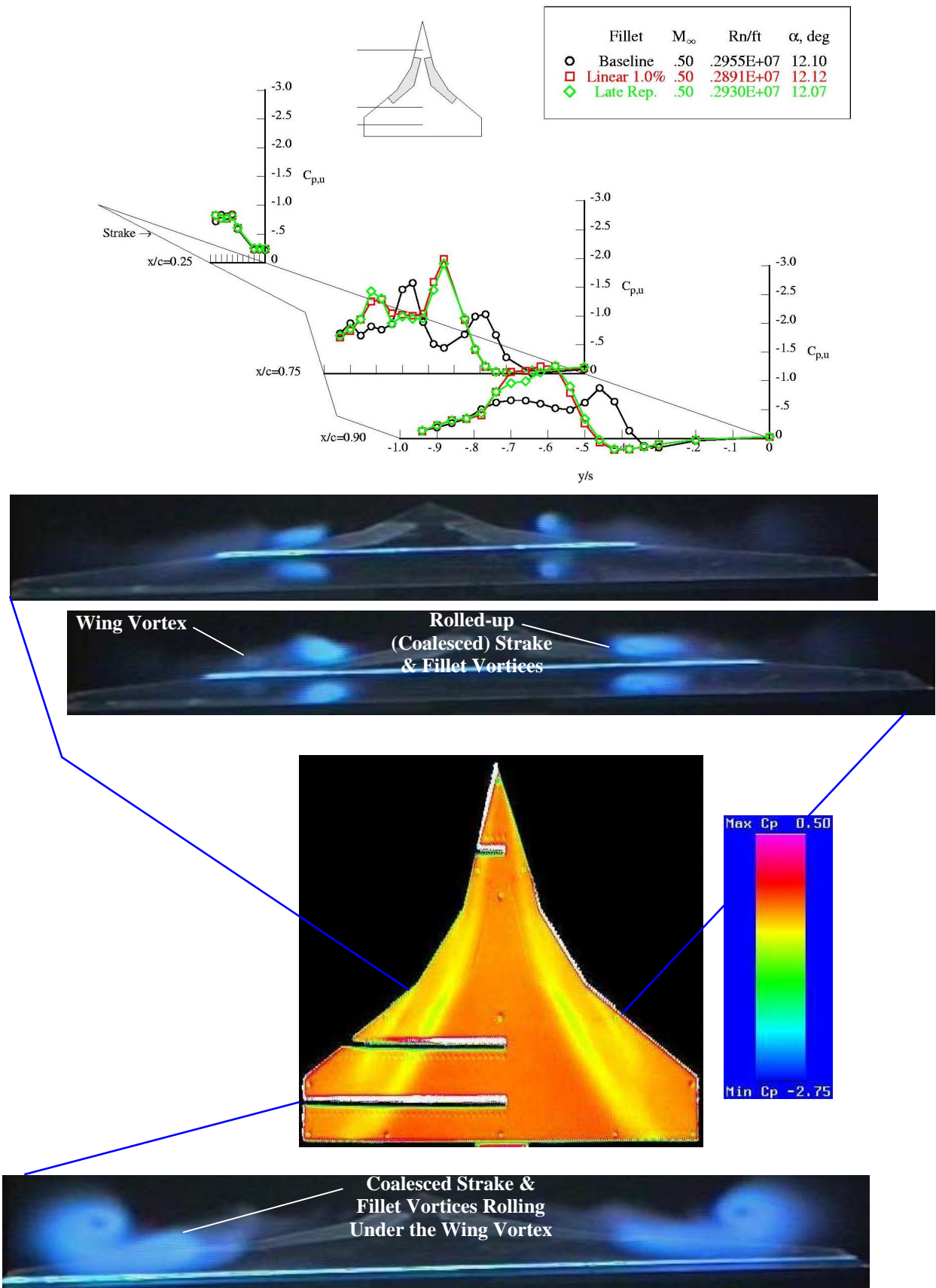


Figure 22 (cont.)- Linear Fillet Flow Field and Pressure Distribution, Mach 0.5, AOA 12°

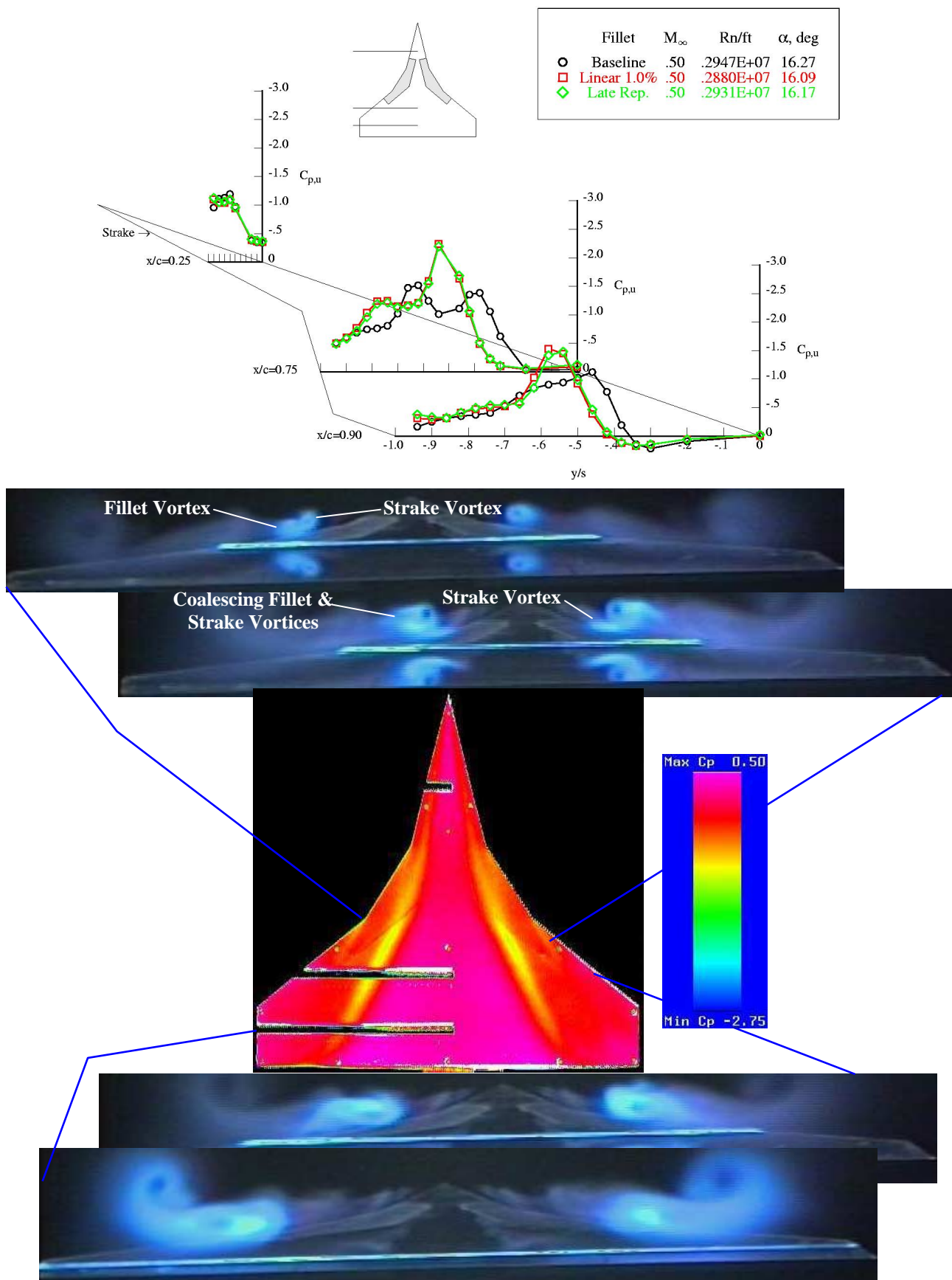


Figure 22 (cont.)- Linear Fillet Flow Field and Pressure Distribution, Mach 0.5, AOA 16°

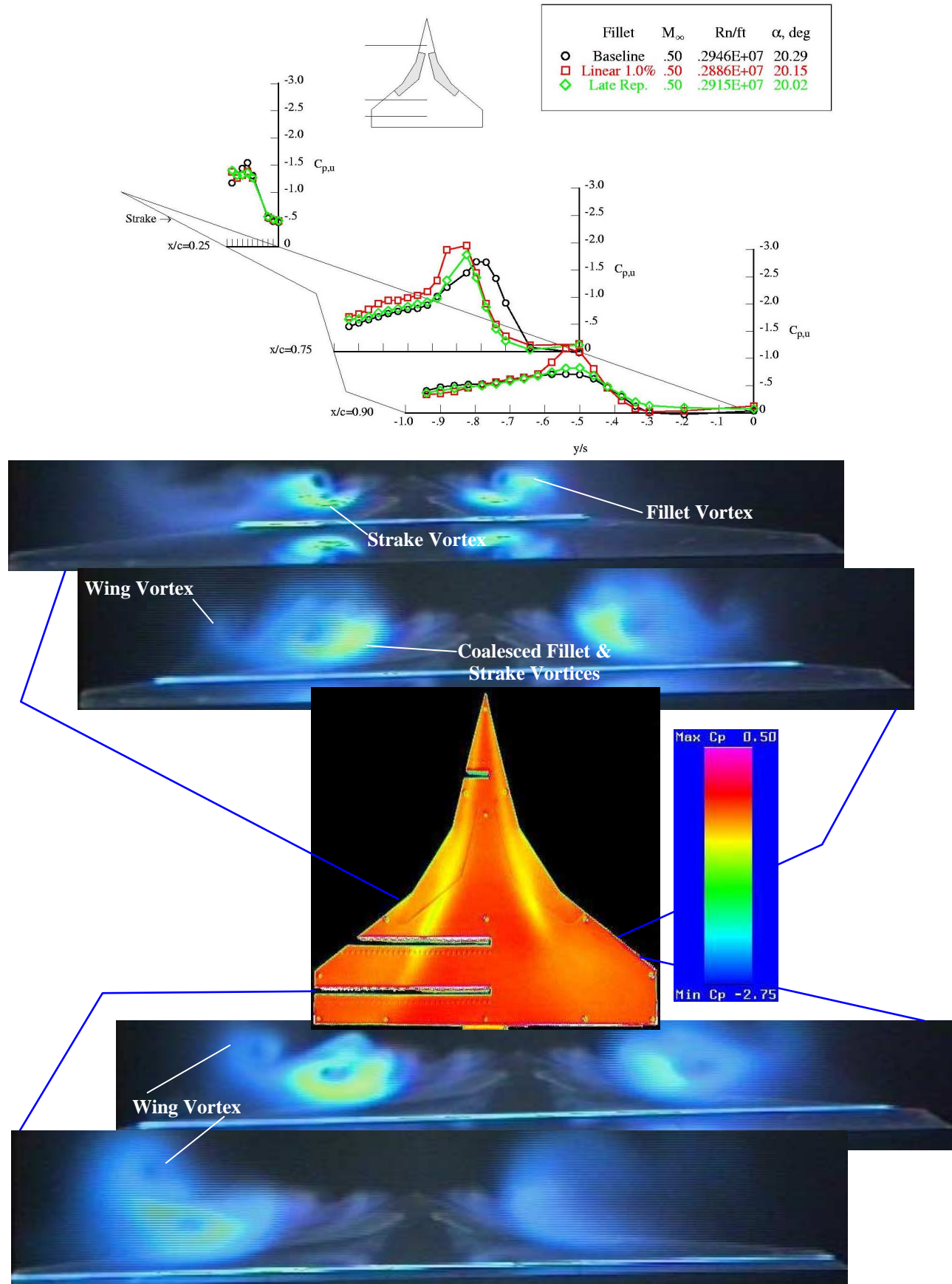


Figure 22 (cont.)- Linear Fillet Flow Field and Pressure Distribution, Mach 0.5, AOA 20°

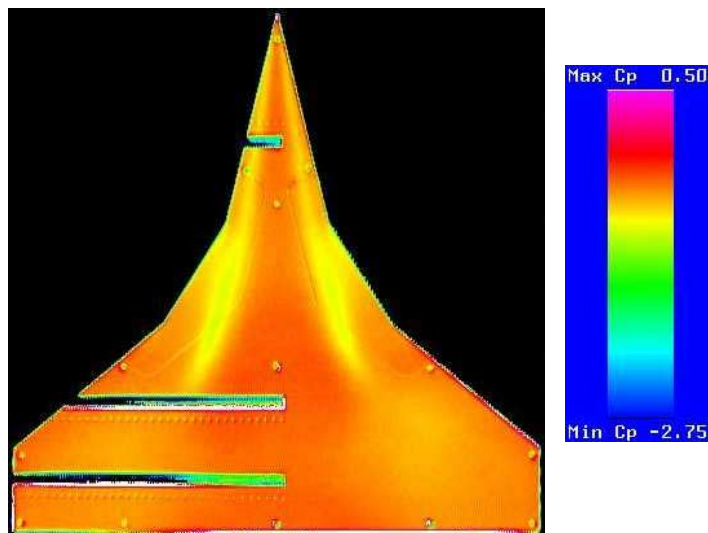
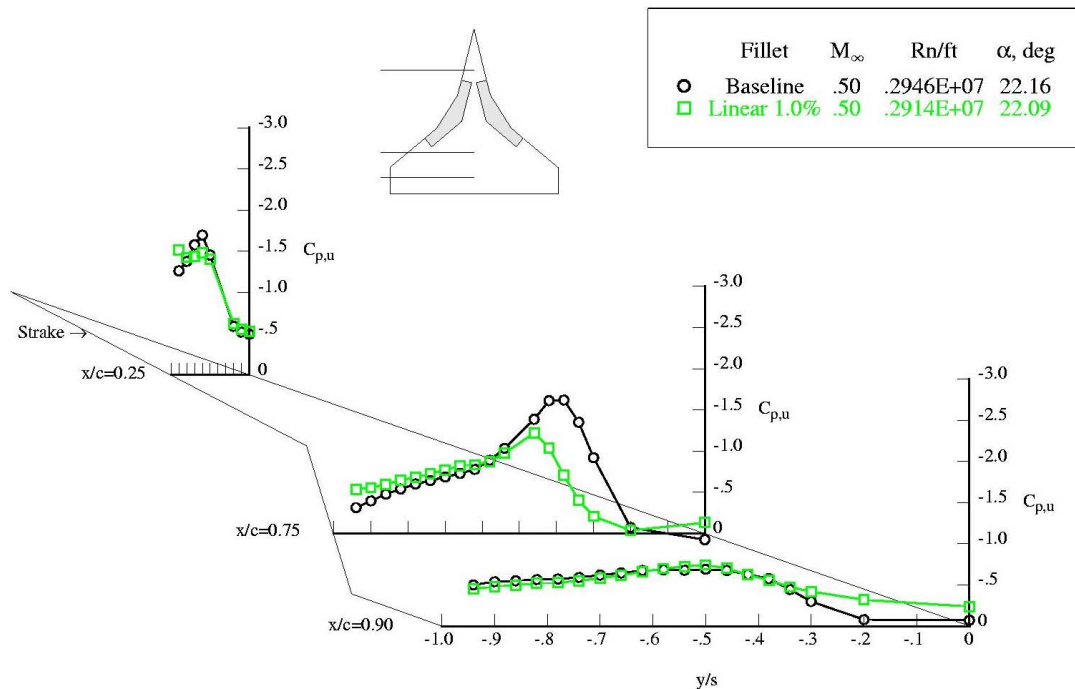


Figure 22 (cont.)- Linear Fillet Flow Field and Pressure Distribution, Mach 0.5, AOA 22°

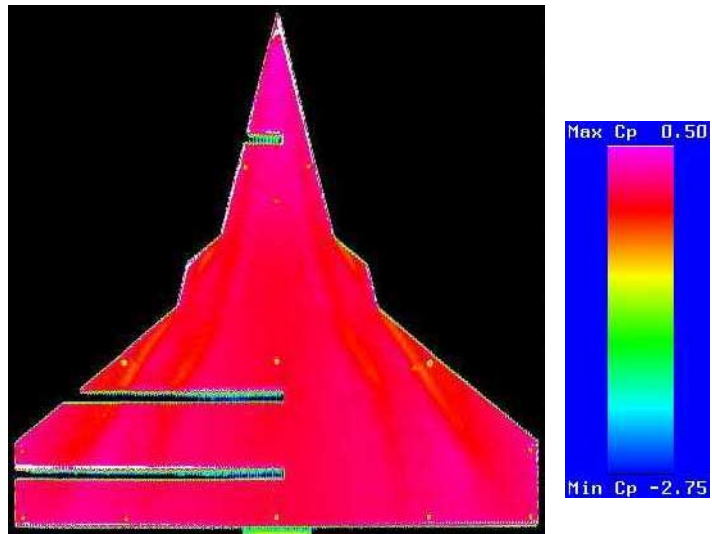
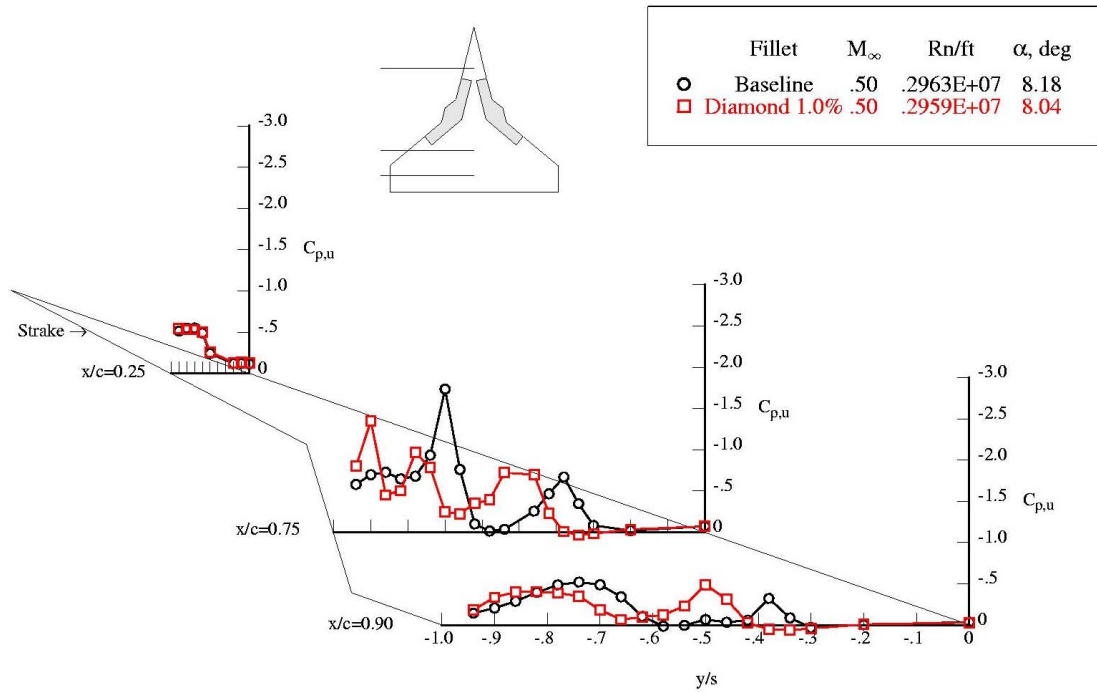


Figure 23- Diamond Fillet Flow Field and Pressure Distribution, Mach 0.5, AOA 8°

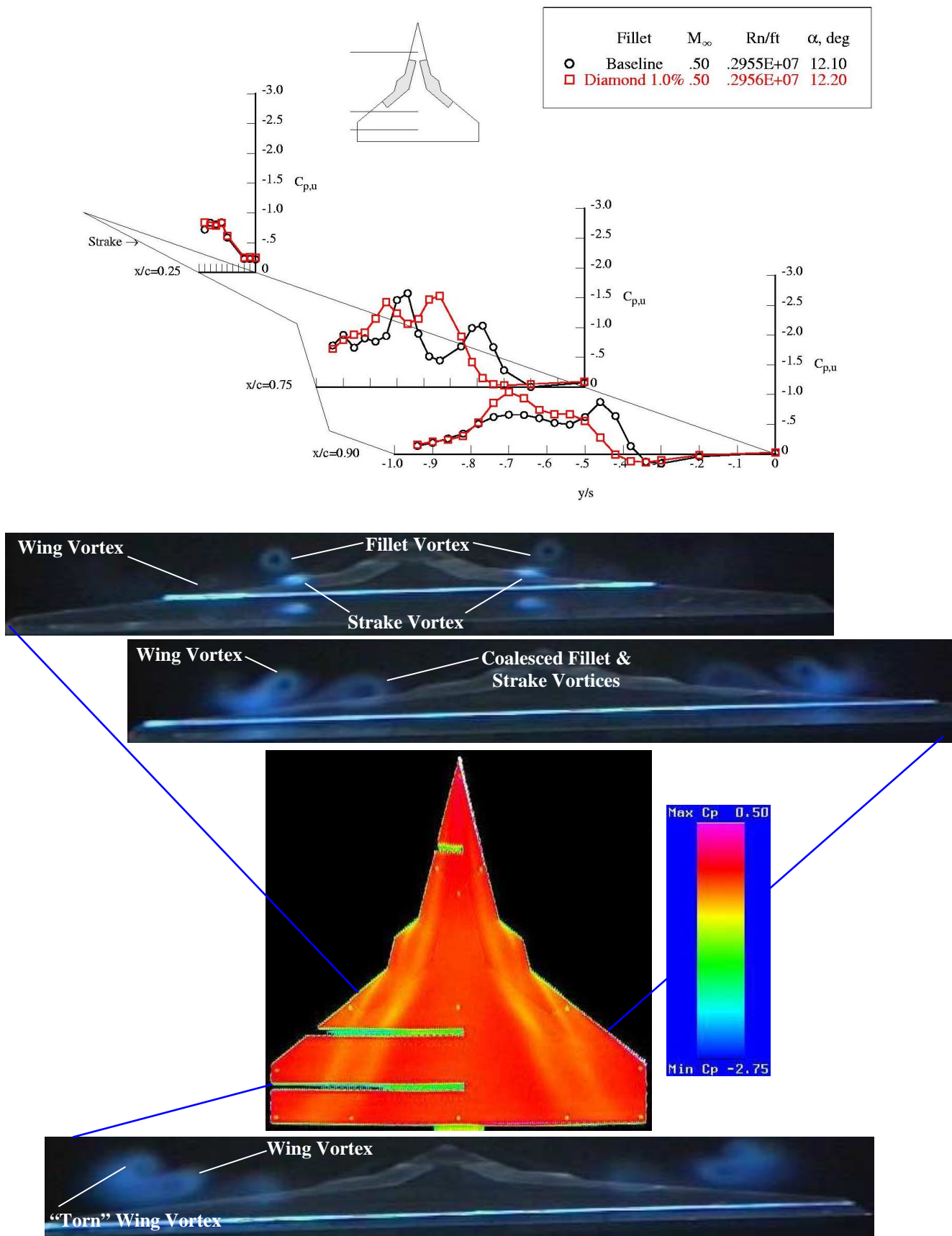


Figure 23 (cont.)- Diamond Fillet Flow Field and Pressure Distribution, Mach 0.5, AOA 12°

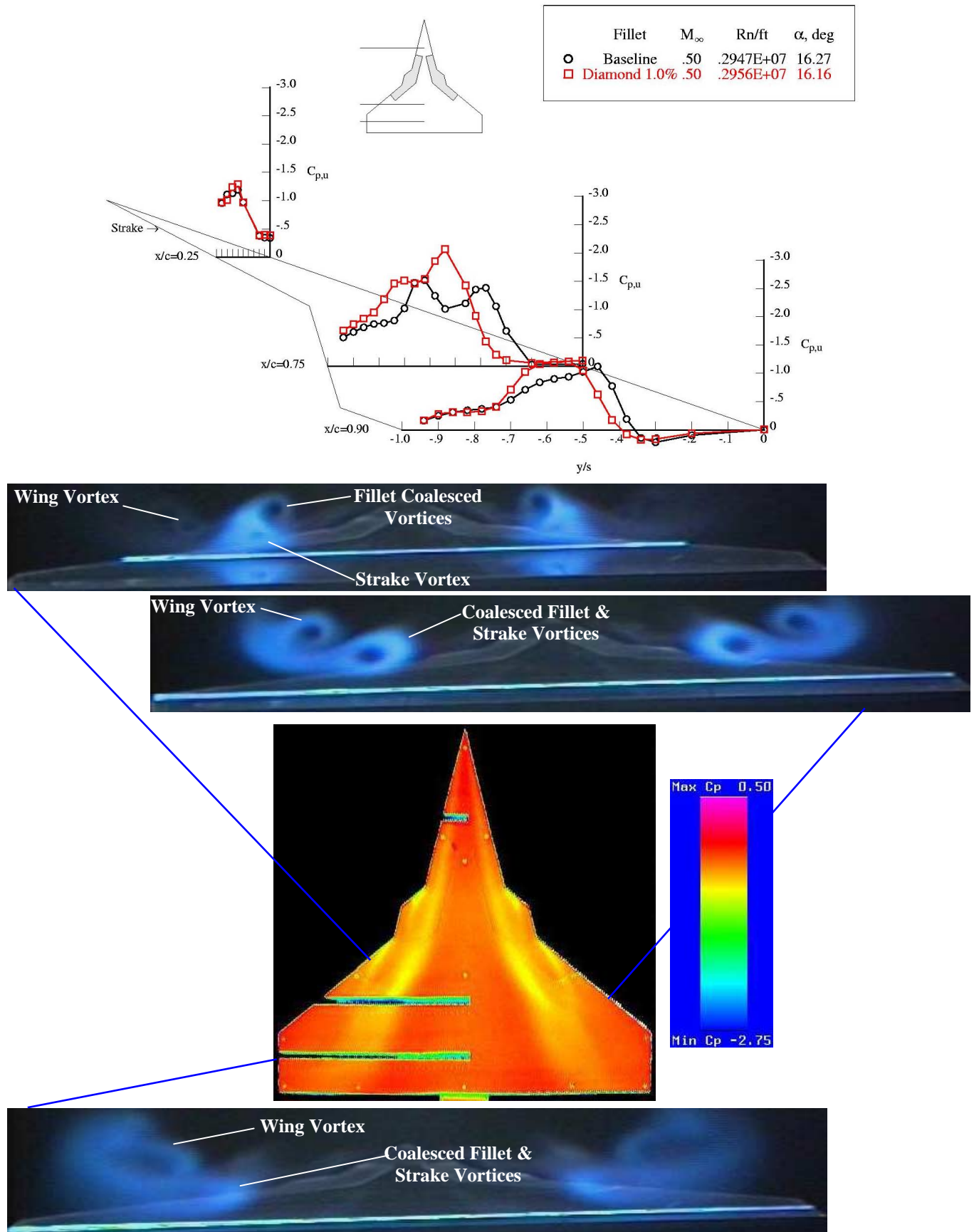


Figure 23 (cont.)- Diamond Fillet Flow Field and Pressure Distribution, Mach 0.5, AOA 16°

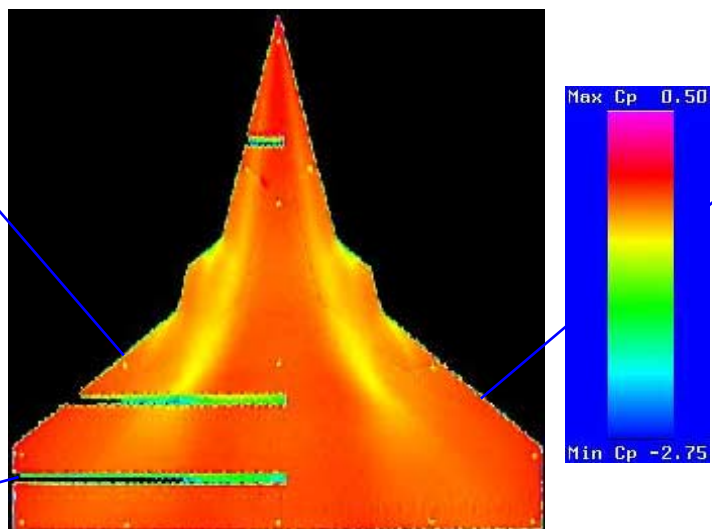
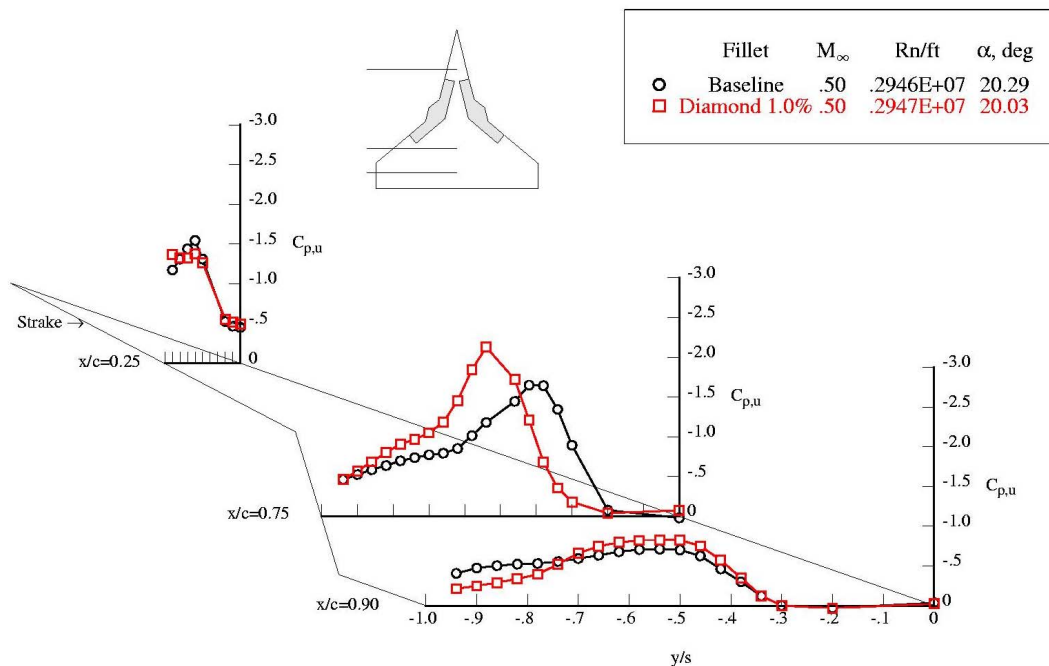


Figure 23 (cont.)- Diamond Fillet Flow Field and Pressure Distribution, Mach 0.5, AOA 20°

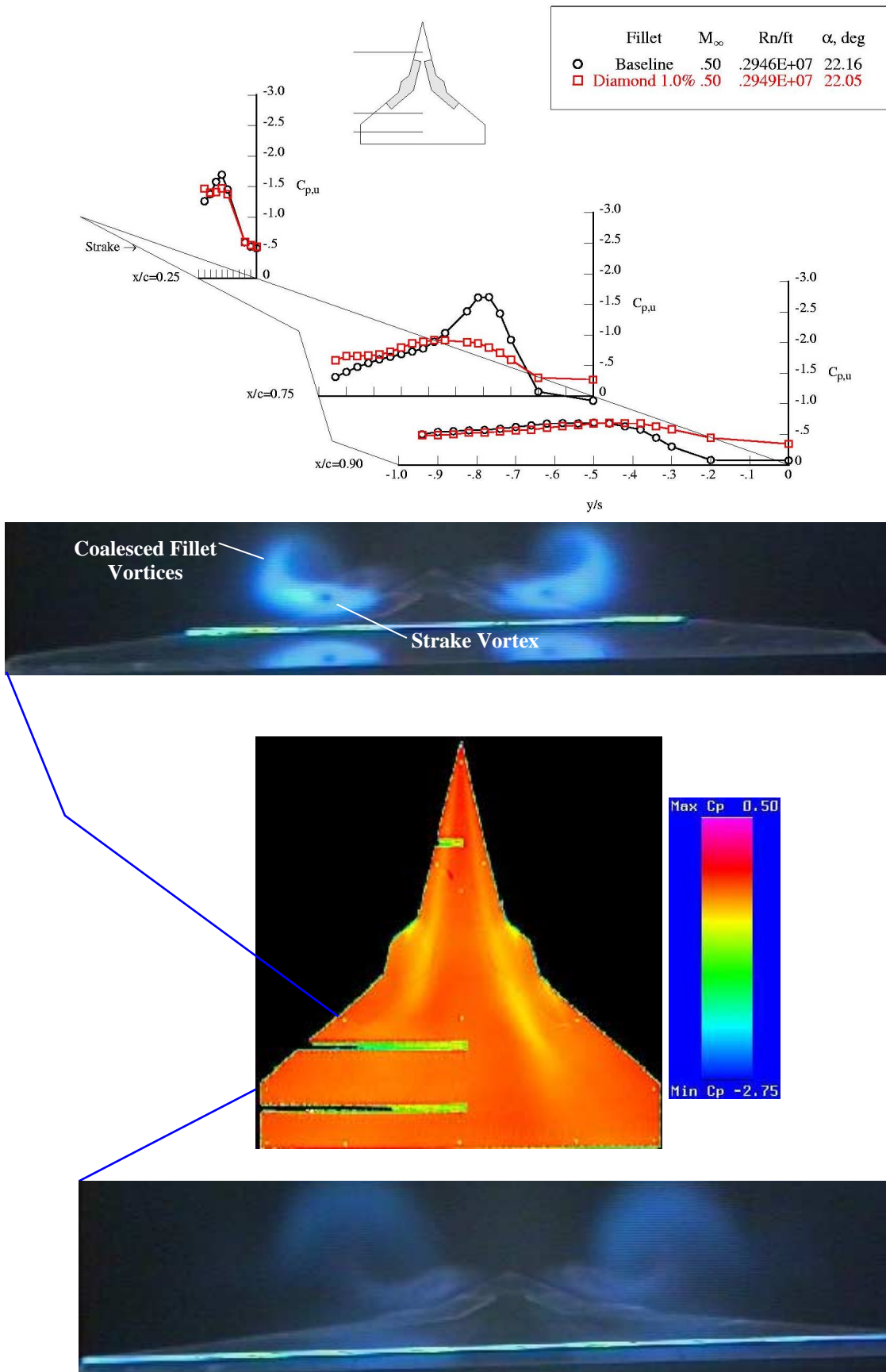


Figure 23 (cont.)- Diamond Fillet Flow Field and Pressure Distribution, Mach 0.5, AOA 22°

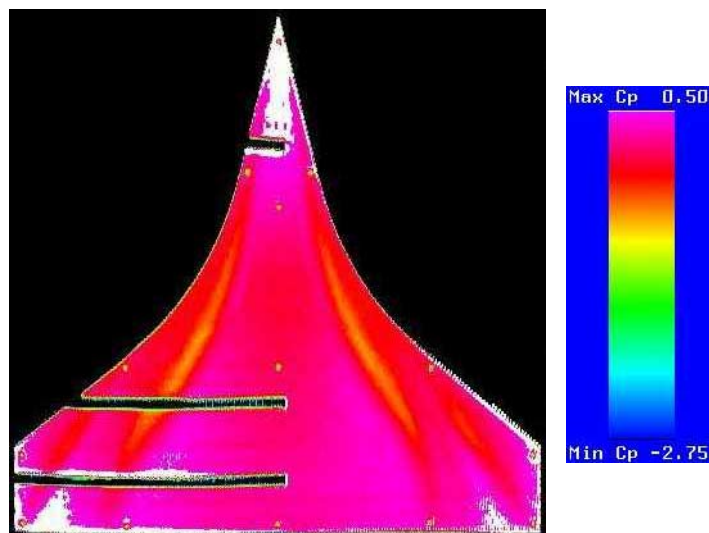
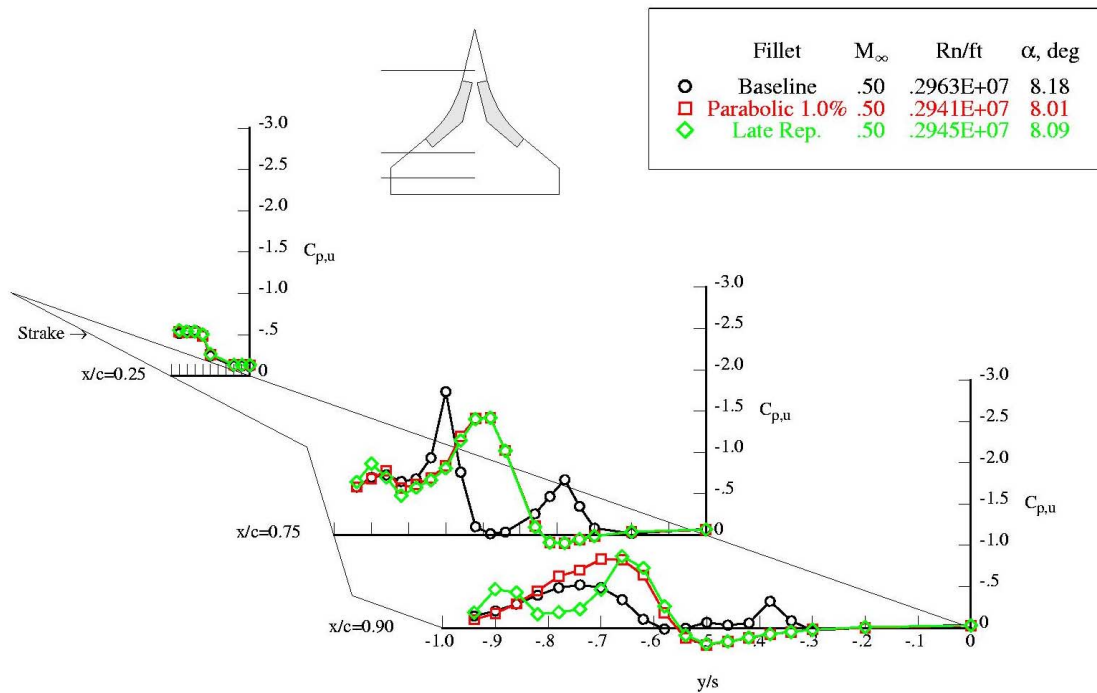


Figure 24- Parabolic Fillet Flow Field and Pressure Distribution, Mach 0.5, AOA 8°

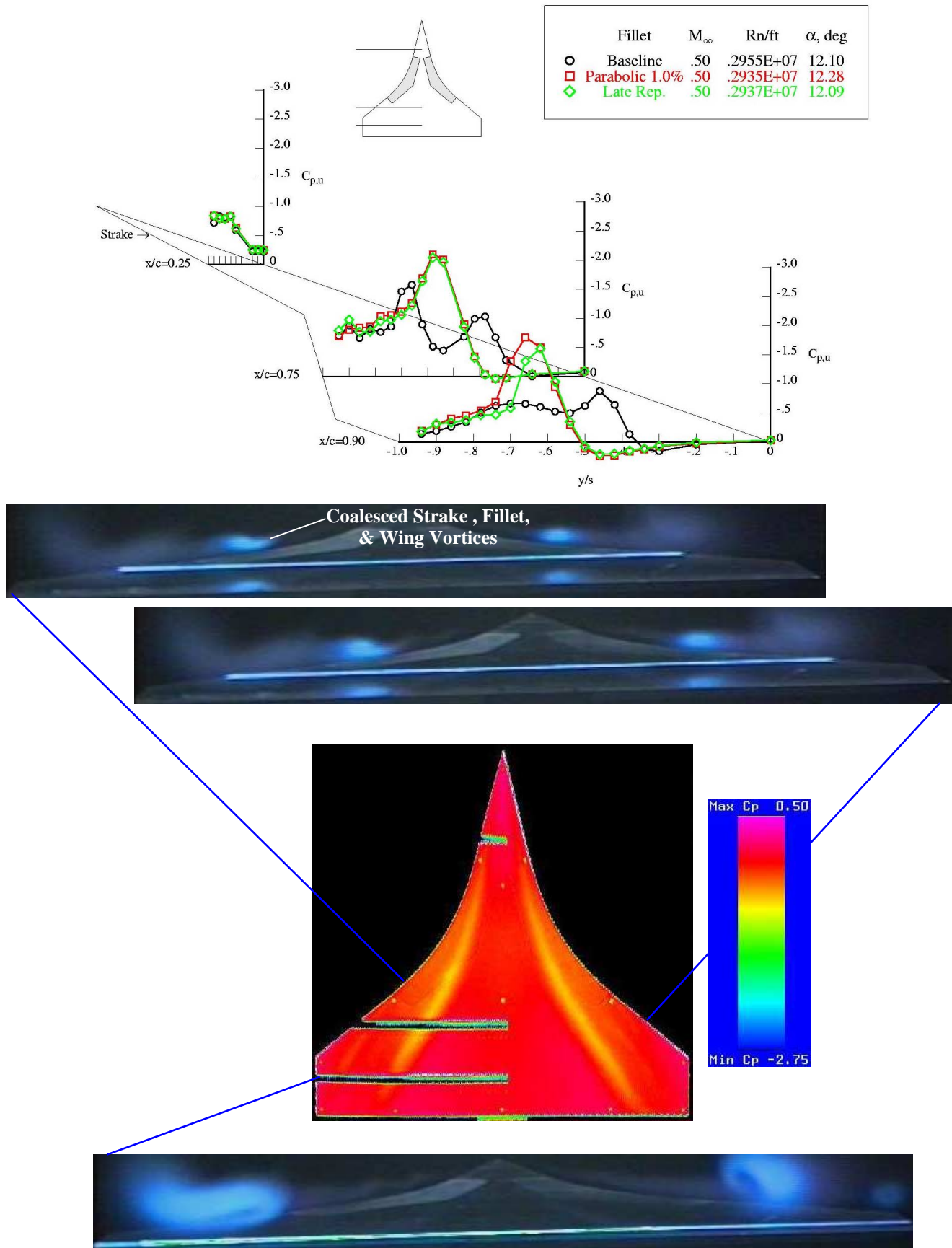


Figure 24 (cont.)- Parabolic Fillet Flow Field and Pressure Distribution, Mach 0.5, AOA 12°

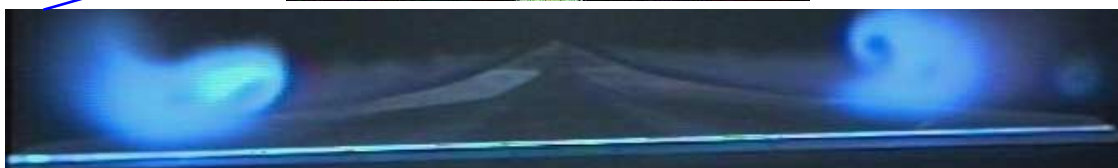
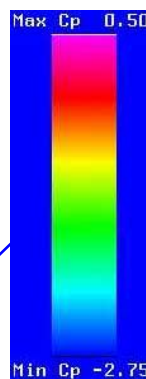
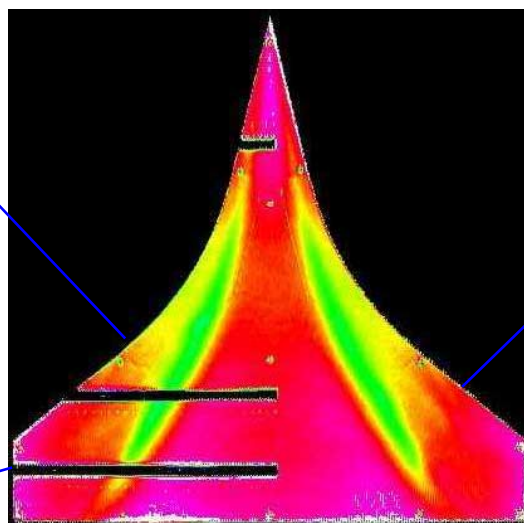
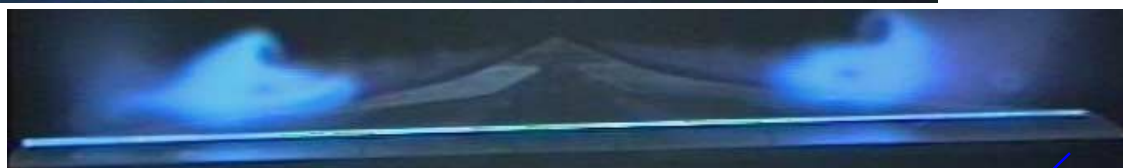
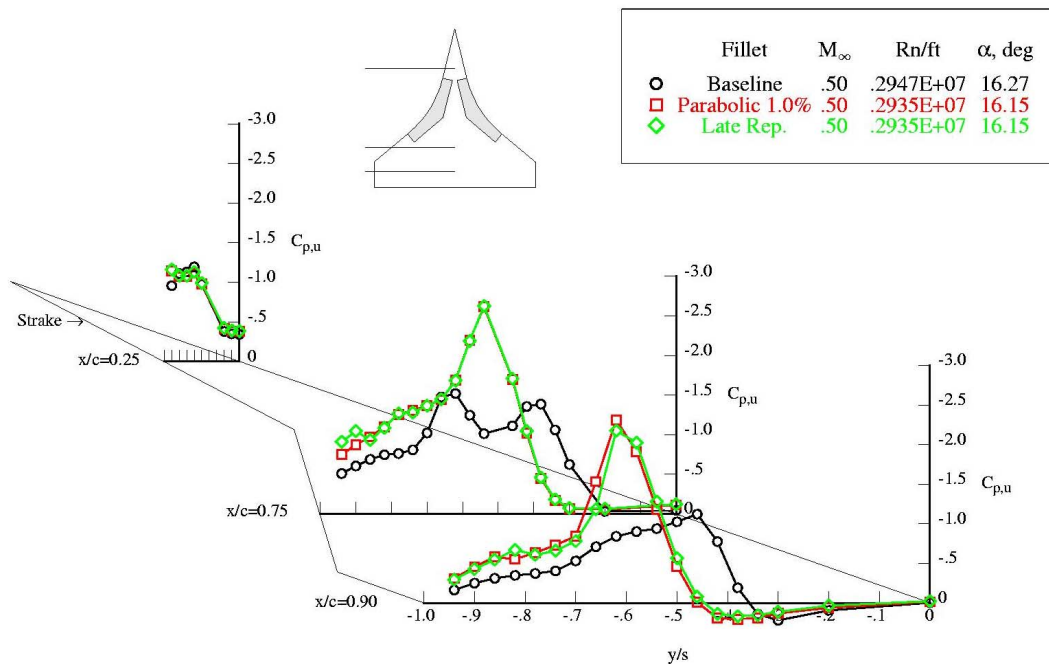


Figure 24 (cont.)- Parabolic Fillet Flow Field and Pressure Distribution, Mach 0.5, AOA 16°

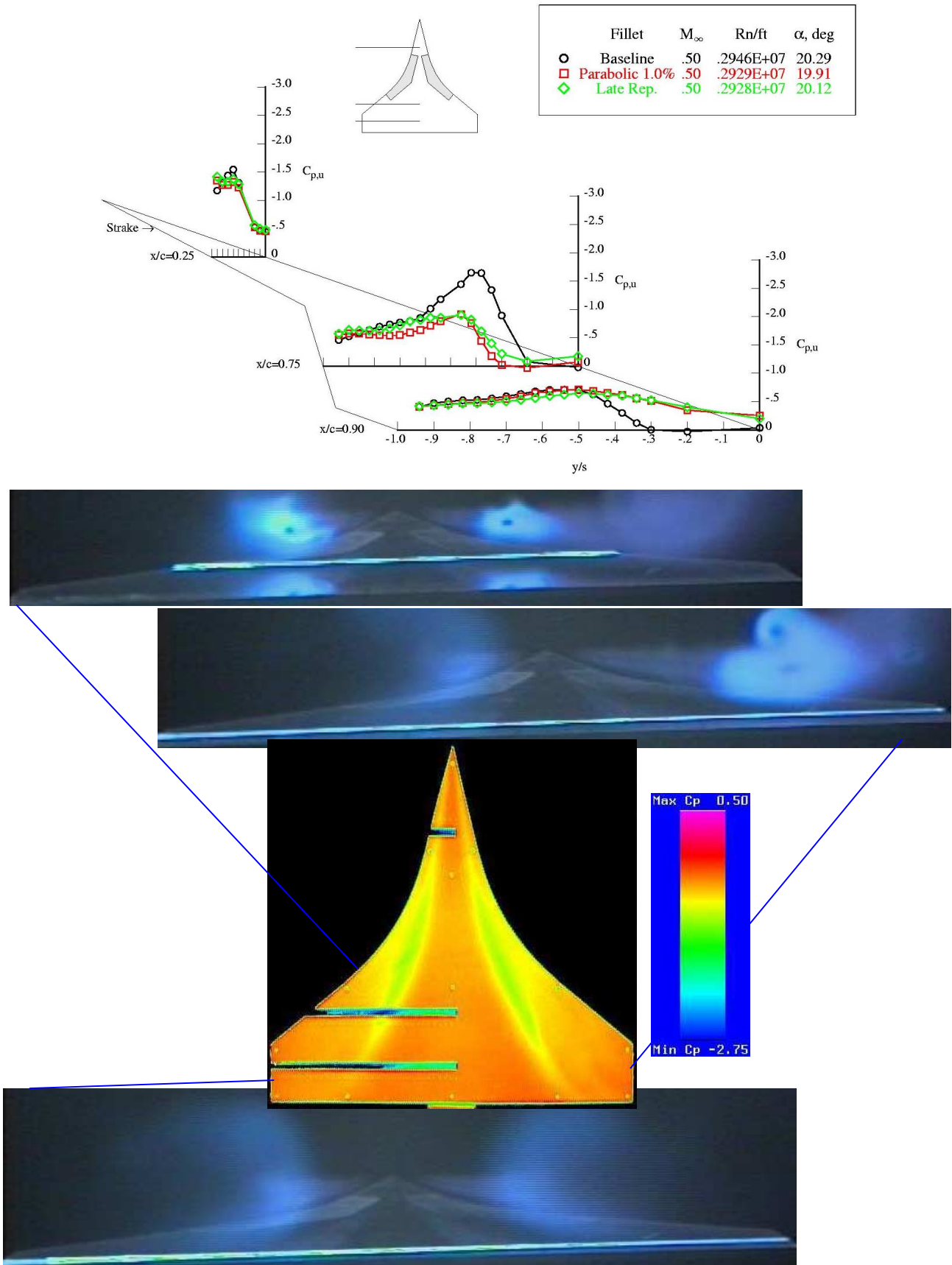


Figure 24 (cont.)- Parabolic Fillet Flow Field and Pressure Distribution, Mach 0.5, AOA 20°

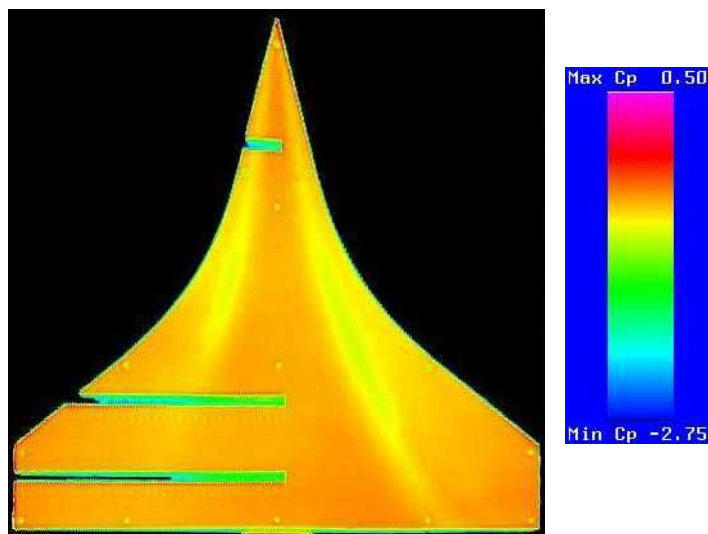
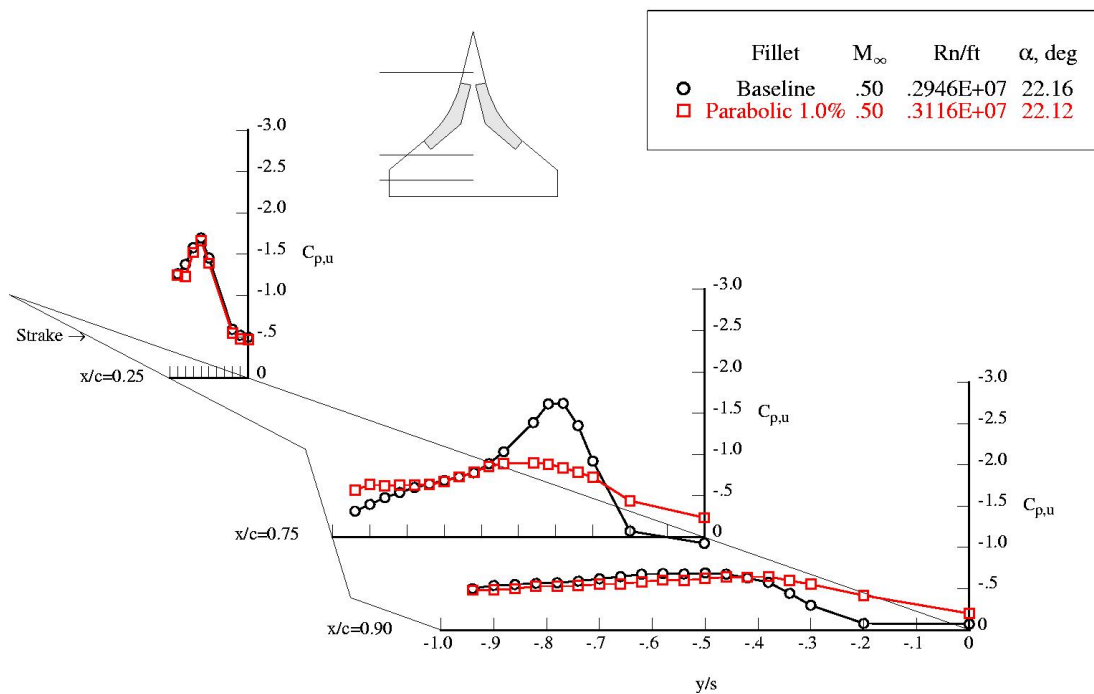


Figure 24 (cont.)- Parabolic Fillet Flow Field and Pressure Distribution, Mach 0.5, AOA 22°

This page has been deliberately left blank



Page intentionnellement blanche